

























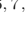





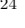



Investigating the sightline of a highly scattered FRB through a filamentary structure in the local Universe

KAITLYN SHIN ^{1,2} CALVIN LEUNG ^{3,*} SUNIL SIMHA ^{4,5} BRIDGET C. ANDERSEN ^{6,7} EMMANUEL FONSECA ^{8,9}
KENZIE NIMMO ¹ MOHIT BHARDWAJ ¹⁰ CHARANJOT BRAR ¹¹ SHAMI CHATTERJEE ¹² AMANDA M. COOK ^{13,14}
B. M. GAENSLER ^{15,14,13} RONNY C JOSEPH ^{6,7} DYLAN JOW ¹⁶ JANE KACZMAREK ¹⁷ LORDRICK KAHINGA ¹⁸
VICTORIA M. KASPI ^{6,7} BIKASH KHAREL ^{8,9} ADAM E. LANMAN ^{1,2} MATTIAS LAZDA ^{13,14} ROBERT A. MAIN ⁶
LLUIS MAS-RIBAS ¹⁸ KIYOSHI W. MASUI ^{1,2} JUAN MENA-PARRA ^{14,13} DANIELE MICHILLI ^{1,2}
AYUSH PANDHI ^{13,14} SWARALI SHIVRAJ PATIL ^{8,9} AARON B. PEARLMAN ^{6,7,†} ZIGGY PLEUNIS ^{19,20}
J. XAVIER PROCHASKA ^{21,22,23} MASOUD RAFIEI-RAVANDI ⁶ MAWSON W. SAMMONS ^{6,7} KETAN R. SAND ^{6,7}
KENDRICK SMITH ²⁴ AND INGRID STAIRS ²⁵

¹MIT Kavli Institute for Astrophysics and Space Research, Massachusetts Institute of Technology, 77 Massachusetts Ave, Cambridge, MA 02139, USA

²Department of Physics, Massachusetts Institute of Technology, 77 Massachusetts Ave, Cambridge, MA 02139, USA

³Department of Astronomy, University of California, Berkeley, CA 94720, United States

⁴Center for Interdisciplinary Research in Astrophysics, Northwestern University, 1800 Sherman Ave., Evanston, IL 60201, USA

⁵Department of Astronomy and Astrophysics, University of Chicago, William Eckhardt Research Center, 5640 South Ellis Avenue, Chicago, IL 60637

⁶Department of Physics, McGill University, 3600 rue University, Montréal, QC H3A 2T8, Canada

⁷Trottier Space Institute at McGill University, 3550 rue University, Montréal, QC H3A 2A7, Canada

⁸Department of Physics and Astronomy, West Virginia University, PO Box 6315, Morgantown, WV 26506, USA

⁹Center for Gravitational Waves and Cosmology, West Virginia University, Chestnut Ridge Research Building, Morgantown, WV 26505, USA

¹⁰McWilliams Center for Cosmology, Department of Physics, Carnegie Mellon University, Pittsburgh, PA 15213, USA

¹¹NRC Herzberg Astronomy and Astrophysics, 5071 West Saanich Road, Victoria, BC V9E2E7, Canada

¹²Cornell Center for Astrophysics and Planetary Science, Cornell University, Ithaca, NY 14853, USA

¹³David A. Dunlap Department of Astronomy & Astrophysics, University of Toronto, 50 St. George Street, Toronto, ON M5S 3H4, Canada

¹⁴Dunlap Institute for Astronomy & Astrophysics, University of Toronto, 50 St. George Street, Toronto, ON M5S 3H4, Canada

¹⁵Department of Astronomy and Astrophysics, University of California Santa Cruz, 1156 High Street, Santa Cruz, CA 95064, USA

¹⁶Kavli Institute for Particle Astrophysics and Cosmology, Stanford University, 452 Lomita Mall, Stanford, CA 94305, USA

¹⁷CSIRO Space & Astronomy, Parkes Observatory, P.O. Box 276, Parkes NSW 2870, Australia

¹⁸Division of Physical and Biological Sciences, University of California Santa Cruz, Santa Cruz, CA 95064, USA

¹⁹Anton Pannekoek Institute for Astronomy, University of Amsterdam, Science Park 904, 1098 XH Amsterdam, The Netherlands

²⁰ASTRON, Netherlands Institute for Radio Astronomy, Oude Hoogeveensedijk 4, 7991 PD Dwingeloo, The Netherlands

²¹Department of Astronomy and Astrophysics, University of California Santa Cruz, Santa Cruz, CA 95064, USA

²²Kavli Institute for the Physics and Mathematics of the Universe (Kavli IPMU), 5-1-5 Kashiwanoha, Kashiwa, 277-8583, Japan

²³Division of Science, National Astronomical Observatory of Japan, 2-21-1 Osawa, Mitaka, Tokyo 181-8588, Japan

²⁴Perimeter Institute for Theoretical Physics, 31 Caroline Street N, Waterloo, ON N2S 2YL, Canada

²⁵Department of Physics and Astronomy, University of British Columbia, 6224 Agricultural Road, Vancouver, BC V6T 1Z1 Canada

ABSTRACT

Fast radio bursts (FRBs) are unique probes of extragalactic ionized baryonic structure as each signal, through its burst properties, holds information about the ionized matter it encounters along its sightline. FRB 20200723B is a burst with a scattering timescale of $\tau_{400\text{MHz}} > 1$ second at 400 MHz and a dispersion measure of $\text{DM} \sim 244 \text{ pc cm}^{-3}$. Observed across the entire CHIME/FRB frequency band, it is the single-component burst with the largest scattering timescale yet observed by CHIME/FRB. The combination of its high scattering timescale and relatively low dispersion measure present an

uncommon opportunity to use FRB 20200723B to explore the properties of the cosmic web it traversed. With an \sim arcminute-scale localization region, we find the most likely host galaxy is NGC 4602 (with PATH probability $P(O|x) = 0.985$), which resides ~ 30 Mpc away within a sheet filamentary structure on the outskirts of the Virgo Cluster. We place an upper limit on the average free electron density of this filamentary structure of $\langle n_e \rangle < 4.6_{-2.0}^{+9.6} \times 10^{-5} \text{ cm}^{-3}$, broadly consistent with expectations from cosmological simulations. We investigate whether the source of scattering lies within the same galaxy as the FRB, or at a farther distance from an intervening structure along the line of sight. Comparing with Milky Way pulsar observations, we suggest the scattering may originate from within the host galaxy of FRB 20200723B.

Keywords: Fast Radio Bursts, Radio transient sources

1. INTRODUCTION

On large scales, ionized matter is found in galaxies, galaxy clusters, and a “cosmic web” of filamentary structures including knots, sheets, and filaments (Bond et al. 1996). Simulations have predicted that this cosmic web can contain around half of the baryons in the Universe (Cen & Ostriker 2006). This ionized matter is often so diffuse that it is challenging to observe even in the local Universe, requiring a patchwork of techniques — such as UV and X-ray absorption spectroscopy, and X-ray emission observations — to probe its emission (e.g., Eckert et al. 2015; Tejos et al. 2016; Nicastro et al. 2018; de Graaff et al. 2019; Tanimura et al. 2019, 2021). As largely extragalactic flashes of radio emission, fast radio bursts (FRBs; Lorimer et al. 2007) provide a way to probe both the column density and density variations of diffuse matter along their sightlines using their observed properties. In particular, the observed dispersion measure (DM) of an FRB quantifies the integral column density of free electrons along the line of sight, and the observed temporal pulse broadening is a result of scattering, which is due to multi-path propagation through inhomogeneous media; the latter property is characterized by a scattering timescale at an observed frequency.

A few earlier studies have demonstrated the power of FRBs to illuminate the physical nature of baryonic structures in our Universe. Prochaska et al. (2019) report on FRB 20181112A, which has an arcsecond localization that intersects the halo of a foreground galaxy, to constrain the diffusiveness of its halo gas. Connor et al. (2020) use FRB 20191108A, which intersects the M31 and M33 halos, to constrain their shared plasma environment properties. Faber et al. (2024) conduct a sightline analysis of FRB 20221219A to propose the burst

could be scattered through the circumgalactic medium (CGM) of an intervening galaxy. Connor et al. (2024) use a sample of cosmological FRBs localized to host galaxies to measure the fraction of baryons in the cosmic web. All of these studies primarily use measurements of dispersion and scattering to constrain ionized baryonic structure difficult to study via other methods.

Here, we report on the CHIME/FRB discovery of FRB 20200723B, a local Universe FRB that resides ≈ 4 virial radii (R_{vir}) away from the center of the Virgo Cluster in the “W-M sheet”, a filamentary structure on the outskirts of the Virgo Cluster (Kim et al. 2016). We use the DM of FRB 20200723B to place constraints on the gas properties of the filamentary structure its host galaxy resides in. Furthermore, we combine the DM with the measured scattering timescale to dissect the line of sight and investigate where the majority of the scatter broadening originates from.

In Section 2, we present the CHIME/FRB discovery of FRB 20200723B and its burst properties. In Section 3, we present the localization region for FRB 20200723B as well as its most probable host galaxy. In Section 4, we discuss the DM budget for the FRB 20200723B sightline, noting its path through the W-M sheet. In Section 5, we discuss the high scattering timescale observed for FRB 20200723B, unusual among bursts observed by CHIME/FRB.

2. FRB 20200723B

2.1. Discovery with CHIME/FRB

The Canadian Hydrogen Intensity Mapping Experiment (CHIME) is a telescope located at the Dominion Radio Astronomical Observatory (DRAO) near Penticton, British Columbia, Canada. CHIME has 1024 dual-polarization antennas across the focal lines of four cylindrical paraboloid reflectors (CHIME Collaboration et al. 2022), and it surveys the entire sky roughly daily at declination $> -11^\circ$ at 400–800 MHz. The CHIME/FRB project is a digital backend on the

* NASA Hubble Fellowship Program (NHFP) Einstein Fellow.

† Banting Fellow, McGill Space Institute (MSI) Fellow, and FRQNT Postdoctoral Fellow.

CHIME telescope. CHIME/FRB discovers $\sim 2\text{-}3$ FRBs per day (CHIME/FRB Collaboration et al. 2021a); such a large discovery rate is enabled by the large field of view and high sensitivity of the CHIME telescope.

In order to identify these FRBs, 1024 fast Fourier transform (FFT) beams are formed and searched for FRBs in real time using their total intensity data, which are at a downsampled time resolution of ~ 1 ms (Ng et al. 2017; CHIME/FRB Collaboration et al. 2018). During the real-time search, Stokes- I intensity data are searched for dispersed signals while the channelized voltage data – baseband data – are stored in a ring memory buffer. All candidate bursts with detection signal-to-noise ratios $S/N > 8$ have intensity data written to disk, but only brighter candidate bursts, e.g., typically with $S/N > 12$, have their baseband data triggered and saved to disk. The baseband data have a time resolution of $2.56 \mu\text{s}$ and typically span ~ 100 ms around the signal of interest, depending on the time of arrival (TOA) and DM values — as well as uncertainty on the DM value — identified by the real-time detection pipeline. Further details on how the baseband data are captured are provided by Michilli et al. (2021) and CHIME/FRB Collaboration et al. (2024).

FRB 20200723B had a real-time detection S/N of ≈ 40.1 , resulting in a baseband dump being successfully triggered. However, only a portion of the burst was caught in baseband. Upon further inspection, this partial capture was likely due to the inaccurate identification of the true DM by the real-time pipeline because of the temporal scatter-broadening, combined with the long duration of the pulse and the shorter timespan of baseband data dump compared to intensity data. Nonetheless, despite us having captured only ~ 100 MHz of signal at the bottom of the CHIME/FRB frequency band, the burst was bright enough to allow for an \sim arcminute scale offline localization and robust probabilistic association with a host galaxy (Section 3). Dynamic spectra of FRB 20200723B using the intensity data and the baseband data can be seen in Figure 1. The wider usable bandwidth and timespan of the lower time resolution intensity data offer much more reliable measurements of the burst properties of FRB 20200723B. Thus, in the following sub-section, we focus on burst properties as observed using intensity data.

2.2. Burst properties

We used a least-squares fitting framework called `fitburst` (Fonseca et al. 2024) to estimate the burst properties of FRB 20200723B. The `fitburst` model fits a pulse broadening function for an intrinsically Gaussian and dispersed pulse; the model parameters con-

sist of the DM, burst TOA, signal amplitude, temporal pulse width, spectral index, spectral running, and scattering timescale τ at a reference frequency, in this case 400.1953125 MHz, the center of the lowest CHIME observing frequency channel (CHIME/FRB Collaboration et al. 2021a). Most `fitburst` measurements for CHIME/FRB bursts typically fix the scattering index assuming $\tau \propto \nu^{-4}$ (e.g., Lorimer & Kramer 2012; CHIME/FRB Collaboration et al. 2021a). As FRB 20200723B is bright and broadband, however, we also use `fitburst` to fit simultaneously for the scattering index.

For FRB 20200723B, `fitburst` measures $DM = 243.99 \pm 0.06 \text{ pc cm}^{-3}$, a scattering index $\alpha = -4.298 \pm 0.065$ and a scattering timescale $\tau_{400 \text{ MHz}} = 1.140 \pm 0.026 \text{ s}$ at the reference frequency. The `fitburst` fit to the intensity data of FRB 20200723B, as well as its model residuals, are shown in Figure 2. This scattering index is closer to -4.4 , the value for a diffractive Kolmogorov scattering model, though it is still in between the values commonly adopted for scattering indexes (-4.0 to -4.4). In practice, many pulsars show a flatter index than expected from diffractive Kolmogorov turbulence (i.e., $\alpha > -4.4$; Rickett et al. 2009; Krishnakumar et al. 2017). If we fix $\alpha = -4$, as was done by CHIME/FRB Collaboration et al. (2021a), we obtain with `fitburst` a $DM = 244.05 \pm 0.06 \text{ pc cm}^{-3}$ and a scattering timescale $\tau_{400 \text{ MHz}} = 1.025 \pm 0.009 \text{ s}$ at the reference frequency. This model fit is marginally worse than the model fit obtained with the scattering index free (using the F-test for model selection, e.g., CHIME/FRB Collaboration et al. 2021a), but we report these numbers for comparison with the larger CHIME/FRB sample. For all analyses through the rest of this paper, we use the values obtained from the `fitburst` fit where we fit for the scattering index as well.

This scattering timescale $\tau_{400 \text{ MHz}} = 1.140 \pm 0.026 \text{ s}$ places FRB 20200723B among the most scattered FRBs discovered. Of all the bursts yet reported by CHIME/FRB, only FRB 20191221A — the FRB source demonstrating sub-second periodicity, with overlapping burst components — has a larger scattering timescale, reported as $\tau_{600 \text{ MHz}} = 340 \pm 10 \text{ ms}$ at 600 MHz (CHIME/FRB Collaboration et al. 2021b). Assuming¹ $\tau \propto \nu^{-4}$, this corresponds to a scattering timescale of $\tau_{400 \text{ MHz}} = 1.721 \pm 0.051 \text{ s}$ at the reference frequency of the bottom of the CHIME observing band.

¹ In the analysis by CHIME/FRB Collaboration et al. (2021b), they fit the integrated profile assumed at 600 MHz; they therefore did not fit for a frequency evolution.

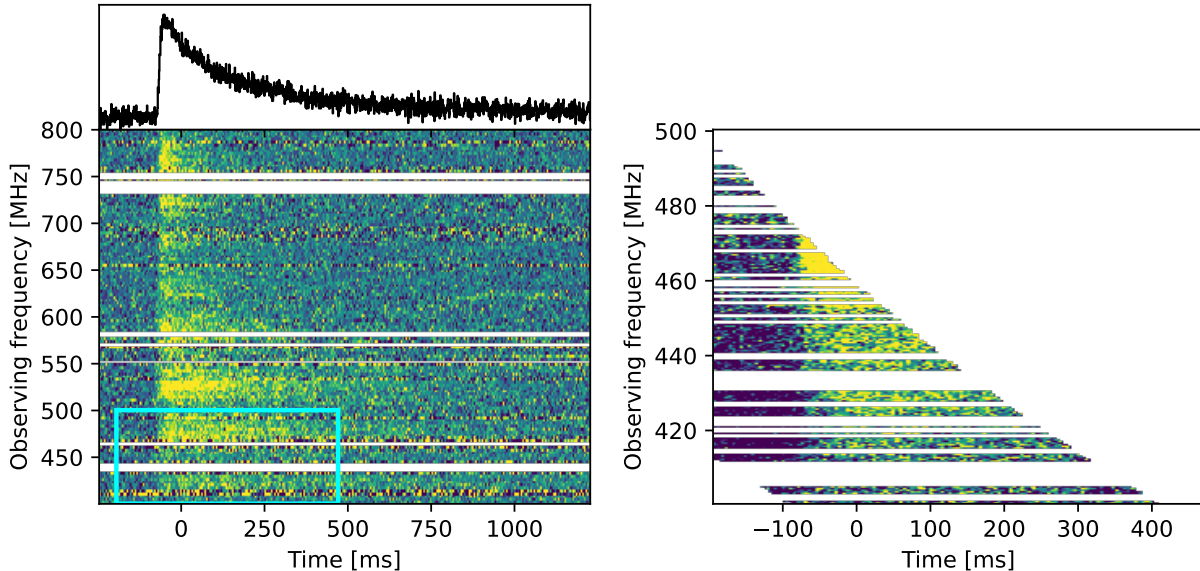


Figure 1. Dynamic spectra of FRB 20200723B as seen with intensity data on the left at 0.983 ms time resolution, and baseband data on the right downsampled to 5.12 ms time resolution from its recorded 2.56 μ s time resolution. The intensity dynamic spectrum is plotted with the frequency channels downsampled by a factor of 8 at a resolution of 3 MHz (showing 128 frequency subbands), over the full 400 MHz observing bandwidth; the baseband dynamic spectrum is plotted at the recorded frequency resolution of 390 kHz, with only the bottom 100 MHz of the data capture shown. The cyan box overlaid on the intensity data subplot corresponds to the extent of the baseband data subplot. Both plots have bands of radio frequency interference (RFI) and missing data masked out. The time axes are referenced to the best-fit TOA from `fitburst`. Due to incorrect real-time detection parameters (e.g., DM and TOA), the baseband system only captured part of the burst. It is clear that the intensity data thus provide a much richer view of the burst properties of this FRB.

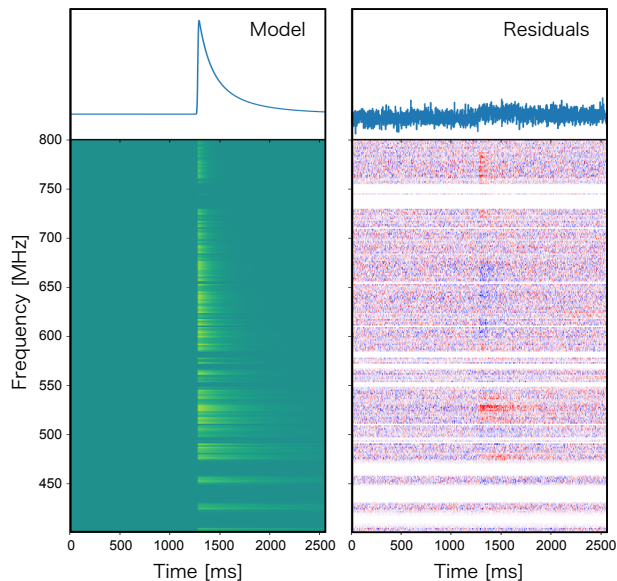


Figure 2. The best-fit `fitburst` model dynamic spectrum for FRB 20200723B (left) alongside the model residuals (right). The model is plot with 256 frequency channels; bands of RFI from the intensity data are masked out in both panels.

2.2.1. Flux/fluence

Estimating fluxes or fluences from CHIME/FRB intensity data is challenging, in large part due to header localization limitations and the complex CHIME/FRB beam model (Andersen et al. 2023). (The header localization is obtained by fitting the detection S/N per formed beam to the frequency-dependent beam model.) As such, the resulting flux and fluence measurements are best interpreted as lower limits, as was the case for the values reported by CHIME/FRB Collaboration et al. (2021a). Using the automated flux calibration software pipeline, we estimate the lower limit on the peak flux of the burst to be $\gtrsim 4.8 \pm 1.4$ Jy, and on the fluence of the burst to be $\gtrsim 820 \pm 213$ Jy ms. All flux and fluence values are band-averaged over the CHIME 400–800 MHz observing frequencies.

This pipeline assumes that the burst was detected along the meridian of the primary beam, a simplifying assumption necessitated by the limited precision of the header localizations; however, due to the captured baseband data for this burst, we are able to get a localization more accurate than the header localization (Section 3). Thus, in theory, our knowledge of the off-meridian position of the FRB should allow for us to correct for the response of the CHIME/FRB primary and

synthesized beam pattern. In practice, however, this burst is detected at a low declination, where the formed FFT beams exhibit more extreme “clamping” structure in the beam shape (Andersen et al. 2023). Thus, while this burst is detected just within the full-width half-max (FWHM) of the primary beam, we find that our formed beam sensitivity to this position is extremely low, especially at frequencies greater than ~ 600 MHz. We therefore do not report an intensity flux/fluence estimate using the baseband localization.

2.2.2. Scintillation

Scintillation is a frequency-dependent variation of intensity due to interference between scattered paths. The scintillation bandwidth, or the decorrelation bandwidth, goes as $\Delta\nu_d \propto \nu^{-\alpha}$. While a single screen can cause both observable scatter-broadening (which goes as $\tau \propto \nu^\alpha$) and scintillation (which can be related to scattering with $\Delta\nu_d \simeq (2\pi\tau)^{-1}$), it is also possible for scattering and scintillation to be contributed by separate screens (e.g., Masui et al. 2015; Ocker et al. 2022b; Sammons et al. 2023; Nimmo et al. 2024). A measurement of scintillation from a different screen than the screen that contributes the scattering can provide possible constraints on the locations of the scattering media along the line of sight. At 1 GHz, the NE2001 Galactic electron density model (Cordes & Lazio 2002) predicts a scatter-broadening of $\tau_{1\text{ GHz}} = 1.2 \times 10^{-4}$ ms, and the expectation for the scintillation bandwidth is $\Delta\nu_d = 1.6$ MHz. Assuming $\alpha = -4.3$, these translate to predictions at 400 MHz of $\tau_{400\text{ MHz}} = 6.0 \times 10^{-3}$ ms and $\Delta\nu_d = 0.03$ MHz. As the observed scattering timescale for FRB 20200723B is greatly in excess of Galactic expectations, it is unlikely for the Milky Way to be the dominant source of observed scattering.

With 16,384 intensity channels across the 400 MHz-wide observing bandwidth of CHIME/FRB, we would be sensitive to spectral “scintles” on scales larger than $\gtrsim 48.8$ kHz. The NE2001 expectation for the scintillation bandwidth at 600 MHz is $\Delta\nu_d \approx 174$ kHz, a scale we should be able to probe with our intensity data. However, any scintillation scale associated with the same extragalactic screen that contributed the large scattering would have a decorrelation bandwidth $\Delta\nu_d < 10^{-3}$ kHz and thus not be resolvable by our intensity data. Importantly, there are artificial frequency variations introduced due to telescope systematics: the original channelization of the baseband data, 400 MHz over 1024 frequency channels, introduces a “scallop” artifact at ~ 0.38 MHz, and there is also an instrumental “ripple” at ~ 30 MHz due to reflections off the feed structure within the CHIME telescope (CHIME Collabora-

tion et al. 2022). When searching the intensity data, no frequency variation scales were found other than the expected artificial variation scales. The NE2001 prediction for scintillation may have been undetected because another screen resolved out the scintillation, or because it was washed out by the instrumental scalloping and correction. It is also possible that a modulation index — a measure of the flux variation caused by scintillation over the bandwidth — that is < 1 could make detection more difficult. Additionally, any intrinsic scintillation with frequency scales around the artificial variation scales, or with frequency scales at finer resolution than 48.8 kHz, cannot be ruled out. It is possible to upchannelize the baseband data to explore scintillation at a finer scale (e.g., Schoen et al. 2021; Nimmo et al. 2024). However, the limited bandwidth of the baseband data for FRB 20200723B limits this analysis.

2.2.3. Polarimetry

FRBs are often highly linearly polarized (e.g., Masui et al. 2015; Pandhi et al. 2024), and linearly polarized radio waves undergo Faraday rotation as they pass through magneto-ionic material. The Faraday rotation measure (RM) is related to the electron number density, n_e , and the line-of-sight (l) component of the magnetic field, B_{\parallel} , by $\text{RM} = 0.8 \int n_e(l) B_{\parallel}(l) dl$ rad m^{-2} . Previous observations of repeating FRBs have shown evidence for a correlation between high RM and strong scattering local to the burst (e.g., Feng et al. 2022; Ocker et al. 2023; Anna-Thomas et al. 2023) as well as the time-variability of the RM itself (Mckinven et al. 2023), suggesting that the RM in at least some sources probes the magneto-ionic environment local to the FRB. Motivated by these results, we measure the RM of FRB 20200723B.

We detect a strong, uncalibrated signal in the Stokes U profile of FRB 20200723B. In large part due to the limited bandwidth of the baseband data capture, we are unable to calibrate the Stokes profiles. For the same reason, the Stokes QU -fitting method of determining the RM fails. This method is more robust against leakage introduced by path length differences in the CHIME telescope system (Mckinven et al. 2021). As such, robust polarization fraction estimates — corrected for leakage — cannot be obtained. However, we are still able to constrain the RM using the baseband data using the RM synthesis method (Burn 1966; Brentjens & de Bruyn 2005) as implemented for CHIME/FRB by Mckinven et al. (2021). This method does not require absolute calibration of the Stokes profiles. The resulting Faraday dispersion function appears to be a convolution of instrumental effects and an astrophysical signal. Thus, over the bottom ~ 100 MHz bandwidth of the baseband

data, we estimate the RM of FRB 20200723B to be $|\text{RM}| < 60 \text{ rad m}^{-2}$. (Using the all-sky map of the Milky Way RM contribution constructed by [Hutschenreuter et al. \(2022\)](#), the Galactic foreground RM expectation is $-5 \pm -6 \text{ rad m}^{-2}$.) This RM value for FRB 20200723B is quite modest, and indicates that the source probably does not originate from an extremely dense and/or strongly magnetized circumburst environment.

3. BURST LOCALIZATION AND HOST GALAXY

Using the baseband localization pipeline ([Michilli et al. 2021](#)), the resulting localization for FRB 20200723B is $\text{RA} = 12\text{h}40\text{m}38(2)\text{s}$, $\text{Dec} = -05^\circ08(1)'06''$ (J2000), with the errors quoted as 1σ uncertainties. Figure 3 shows this localization region overlaid on archival imaging from the Dark Energy Camera Legacy Survey (DECaLS; [Dey et al. 2019](#)). Clearly evident in the localization region is the bright putative host galaxy, NGC 4602, a Seyfert spiral galaxy ([Tommasin et al. 2010](#)). This galaxy is included in the HI Parkes All-Sky Survey (HIPASS) catalog ([Meyer et al. 2004](#)); the reported neutral hydrogen radial velocity measurements imply a redshift of $z = 0.0085$. This redshift is consistent with what has been found with optical and mid-infrared spectroscopy ([Tommasin et al. 2008](#); [Feltre et al. 2023](#)). The redshift-inferred distance, using *Planck* cosmological parameters ([Planck Collaboration et al. 2020](#)), is ~ 37.59 Mpc. This galaxy also has a redshift-independent distance as derived by the Tully-Fisher relation ([Tully & Fisher 1977](#)). Converting from the reported best-fit distance modulus, NGC 4602 is $32.49^{+2.87}_{-2.64}$ Mpc away, with an inclination angle of $i = 73 \pm 3^\circ$ ([Kourkchi et al. 2020](#)). Throughout this paper, we will use the redshift-independent distance when referring to NGC 4602, as it is more robust against peculiar velocity effects when inferring distance (e.g., [Steer et al. 2017](#)). This host galaxy distance of ≈ 32.5 Mpc places FRB 20200723B among the closest reported FRBs; other notably nearby FRBs include FRB 20200120E at ≈ 3.6 Mpc ([Bhardwaj et al. 2021a](#); [Kirsten et al. 2022](#)) and FRB 20181030A at ≈ 20 Mpc ([Bhardwaj et al. 2021b](#)). A further analysis and discussion of the host galaxy properties of NGC 4602 will be presented as part of a larger sample by [Andersen et al.](#) (in prep.).

We can also obtain a probabilistic maximum redshift for an FRB given its observed DM, i.e., $P(z|\text{DM})$. While both [Shin et al. \(2023\)](#) and [James \(2023\)](#) model $P(z|\text{DM})$ for CHIME/FRB based on observations from the first CHIME/FRB catalog, [Shin et al. \(2023\)](#) explicitly exclude highly scattered FRBs in their modeling. Thus, we use the work by [James \(2023\)](#), who include

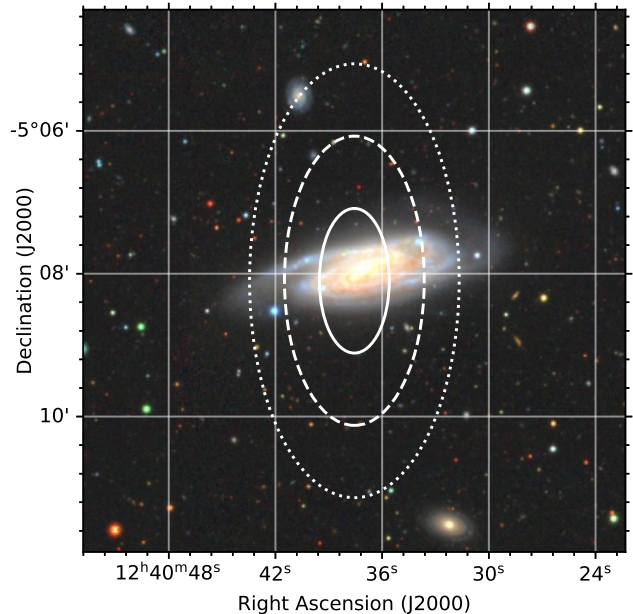


Figure 3. The 1σ (solid ellipse), 2σ (dashed ellipse), and 3σ (dotted ellipse) baseband localization regions for FRB 20200723B, plotted on top of archival DECaLS imaging in the *grz* bands. The central galaxy, and the putative host of FRB 20200723B, is NGC 4602 at $z = 0.0085$.

highly scattered FRBs in their modeling, and provide a joint probability distribution of redshift and extragalactic DM, $P(z, \text{DM}_{\text{EG}})$.² We can go from the joint probability distribution to the conditional probability distribution via $P(z|\text{DM}_{\text{EG}}) = P(z, \text{DM}_{\text{EG}})/P(\text{DM}_{\text{EG}})$. Subtracting the NE2001 ([Cordes & Lazio 2002](#)) model for the Galactic DM contribution to FRB 20200723B, we obtain a DM_{EG} contribution of $\approx 210 \text{ pc cm}^{-3}$. The 95% upper limit of $P(z|\text{DM}_{\text{EG}} = 210 \text{ pc cm}^{-3})$ is $z \approx 0.32$. The redshift of NGC 4602, at $z = 0.0085$, is comfortably within the range of redshifts one would expect based on its extragalactic DM, i.e., consistent with $z \leq 0.32$.

With NGC 4602 located so prominently within the 1σ baseband localization region of FRB 20200723B at a redshift allowed by the observed DM, it is qualitatively unlikely for any other galaxy to be the host galaxy for this FRB. Nevertheless, this association of FRB 20200723B with NGC 4602 can be assessed with the Probabilistic Association of Transients to their Hosts (PATH) method ([Aggarwal et al. 2021](#)). PATH is a Bayesian framework which assigns association probabilities to each galaxy in a provided flux-limited catalog. We use DECaLS as our galaxy catalog, as it is the deepest survey covering the

² Available in the FRBs repository at https://github.com/FRBs/zdm/blob/99aed43/docs/nb/CHIME_pzDM.ipynb.

localization region of FRB 20200723B. Based on sand-boxing simulations with host galaxy associations using PATH and CHIME/FRB baseband localization regions (Andersen et al. in prep.), we adopt an unseen prior³ $P(U) = 0.15$. The resulting posterior association probability for NGC 4602 is $P(O|x) = 0.985$, a probabilistically robust host galaxy association. No other galaxy detected by DECaLS has a posterior association probability of $P(O|x) > 0.005$.

4. LINE OF SIGHT CONTRIBUTIONS TO THE DM

In this section, we quantify possible contributions to the DM of FRB 20200723B from media along its line of sight, noting that there is also a local Universe filamentary structure along the sightline of this burst.

4.1. The W-M sheet

The nearest galaxy cluster to NGC 4602, both in 3D and projected on the sky, is the Virgo Cluster, which has a virial radius $R_{\text{vir}} = 1.08$ Mpc (Urban et al. 2011). Reiprich et al. (2013) define the outskirts of clusters to be out to $3R_{\text{vir}}$. As the impact parameter between NGC 4602 and the Virgo Cluster is $b_{\perp} \sim 4.4$ Mpc $> 3R_{\text{vir}}$, there is likely a negligible amount of the intra-cluster medium (ICM) by NGC 4602. Thus, we expect any potential ICM contribution to the total observed DM of FRB 20200723B to be negligible. However, NGC 4602 appears to be part of a filamentary structure associated with the outskirts of the Virgo Cluster; this structure is called the “W-M sheet” (Kim et al. 2016). Although the exact data comprising the discovered W-M sheet structure were not made public, because NGC 4602 is at a distance < 40 Mpc from Earth, we expect the galaxies in the W-M sheet to be encompassed by the latest NED Local Volume Sample (NED-LVS 2021-09-22v2; Cook et al. 2023b), which contains galaxies with distances out to 1000 Mpc. To confirm that NGC 4602 is *within* the W-M sheet, we query the NED-LVS for galaxies with projected positions within ± 2.5 degrees of the center of NGC 4602 and at a redshift $z > 0.007$ to look for spatial clustering. Indeed, we identify a sub-group of 12 galaxies (including NGC 4602)⁴

³ This unseen prior, $P(U)$ corresponds to the probability that the true host galaxy of the FRB is unseen within the adopted galaxy survey. Typical values in the literature adopt $P(U) = 0.1$ when using DECaLS as the galaxy survey (e.g., Ibik et al. 2024), but Andersen et al. (in prep.) found that a higher unseen prior probability was more representative for associations using CHIME/FRB localization regions.

⁴ There are far more galaxies in the W-M sheet than this subsample of galaxies, but we were interested only in verifying that NGC 4602 is indeed associated with the W-M sheet, for which only a local subset of galaxies is needed.

that appear clustered at similar redshifts, and are also within the 3D structural extent of the W-M sheet provided by Kim et al. (2016). We note that Castignani et al. (2022) also independently confirmed the W-M sheet structure, but their sample selection only extends down to declination -1.3° , and thus does not include NGC 4602 which is at a declination of -5.13° .

Of particular interest is the contribution to the DM of FRB 20200723B from this W-M sheet. With an estimate of the distance that this burst traveled *through* the W-M sheet to its front face (relative to Earth), we can thus use DM budgeting to place constraints on the free electron density of this filamentary structure. We use the Cartesian supergalactic coordinates provided by Kim et al. (2016) to estimate the physical extent of the W-M sheet. The supergalactic coordinate system is referenced to the “supergalactic plane”, i.e., the plane of the Local Supercluster (Peebles 2022); this is a great circle traced across the sky in the local Universe within which there appears to be a concentration of extragalactic matter (de Vaucouleurs 1971). In the Cartesian supergalactic coordinate system, SGX and SGY axes are in the supergalactic plane, with the SGZ axis pointing towards the north supergalactic pole and the Earth at the origin. The SGY axis, around the Virgo Cluster, approximately corresponds to the line of sight (Castignani et al. 2022). These coordinates are often specified in units of h^{-1} Mpc.

The provided coordinate ranges of the W-M sheet are given as $(\text{SGX}, \text{SGY}, \text{SGZ}) = (-13.38 \sim -1.66, 16.03 \sim 24.99, -3.10 \sim -1.10) h^{-1}$ Mpc.⁵ Towards the direction of the W-M sheet from Earth, the range of SGX–SGZ coordinates at the maximum SGY value roughly span a plane marking the start of the filamentary W-M sheet structure. Adopting *Planck* cosmological parameters (Planck Collaboration et al. 2020) for the supergalactic coordinates, where $H_0 = 100 h$ km s⁻¹ Mpc⁻¹ and $h = 0.6766$, we use singular value decomposition to obtain a best-fit plane to the coordinates of the W-M sheet closest to Earth. From NGC 4602 along the line of sight, we can find the point of intersection with the front face of the W-M sheet (relative to Earth). The distance FRB 20200723B would have traversed, from NGC 4602 through the W-M sheet, is thus $3.9_{-2.6}^{+2.9}$ Mpc. A visualization of the geometry between NGC 4602, the front face of the W-M sheet relative to Earth, and the line of sight between NGC 4602 and Earth can be seen in Figure 4.

⁵ This filamentary structure is elongated along the SGY axis, hence the designation “W-M sheet” instead of “W-M filament” (Kim et al. 2016).

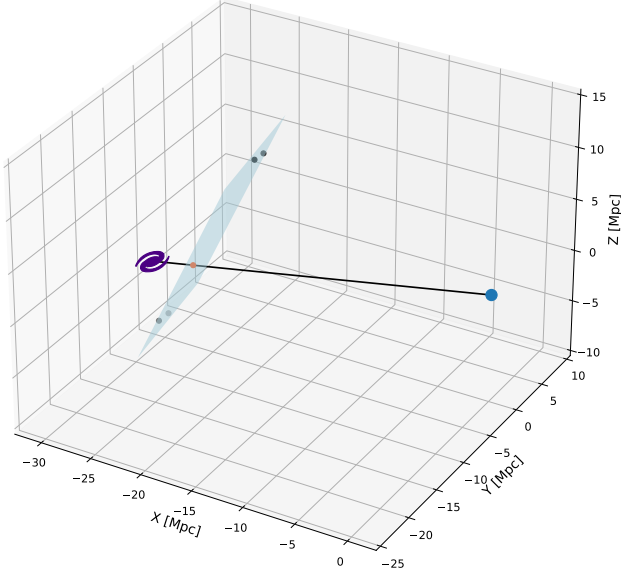


Figure 4. A 3D visualization, in Cartesian coordinates, of the best-fit plane (light blue sheet) of the front face of the W-M sheet between NGC 4602 (purple spiral galaxy icon) and Earth (blue dot). We emphasize that NGC 4602 is *within* the W-M sheet, and that the full volumetric extent of the W-M sheet, including its back face, is not depicted in this plot. We use the redshift-independent Tully-Fisher distance measurement for NGC 4602. The plane is fit to the four points spanning the corners of front face of the W-M sheet (black dots); for added visualization effect, the plane is plotted slightly past these points. Along the line of sight between NGC 4602 and Earth (straight black line), the point of intersection with the best-fit plane of the front face of the W-M sheet is plotted in orange. The distance from NGC 4602 to the point of intersection is $3.9^{+2.9}_{-2.6}$ Mpc.

4.2. DM budgeting

We split the DM of FRB 20200723B into its line of sight components, aiming to place constraints on the DM contribution from the W-M sheet. Given that NGC 4602 is in the local Universe, we ignore factors of $1+z$. The DM for FRB 20200723B can thus be broken into

$$\begin{aligned} \text{DM} = & \text{DM}_{\text{mw,disk}} + \text{DM}_{\text{mw,halo}} + \text{DM}_{\text{igm}} \\ & + \text{DM}_{\text{int,halos}} + \text{DM}_{\text{sheet}} + \text{DM}_{\text{h}} \quad (1) \end{aligned}$$

where $\text{DM}_{\text{mw,disk}}$ is the interstellar medium (ISM) contribution from the Milky Way (MW); $\text{DM}_{\text{mw,halo}}$ is the MW halo contribution; DM_{igm} is the diffuse intergalactic medium (IGM) contribution; $\text{DM}_{\text{int,halos}}$ is the contribution from intervening galaxy halos along the line of sight; DM_{sheet} is the contribution from the W-M sheet; and DM_{h} is the host galaxy contribution. To maximize the simplicity of the methodology and the conservatism of the constraints, we adopt uniform distributions (with

very generous edges) for the probability distributions for each of these DM components.

For estimating the MW disk contribution to the DM of FRB 20200723B, there are two Galactic electron density models to consider — the NE2001 (Cordes & Lazio 2002) model and the YMW16 model (Yao et al. 2017). Towards FRB 20200723B, the NE2001 prediction is $\sim 33 \pm 7 \text{ pc cm}^{-3}$, while the YMW16 prediction is $\sim 25 \pm 5 \text{ pc cm}^{-3}$. We take the 2σ value below the YMW16 prediction and the 2σ value above the NE2001 prediction to denote the edges of our probability distribution for the MW disk contribution to the total DM. Thus, $\text{DM}_{\text{mw,disk}} \in [15, 47] \text{ pc cm}^{-3}$.

Estimates for the MW halo contribution to the DM span $\approx 10\text{--}80 \text{ pc cm}^{-3}$ (e.g., Dolag et al. 2015; Prochaska & Zheng 2019; Keating & Pen 2020). As some halo models may overestimate MW halo DM contributions, as discussed by Cook et al. (2023a), we conservatively adopt a range $\text{DM}_{\text{halo}} \in [10, 80] \text{ pc cm}^{-3}$.

As NGC 4602 is only ≈ 32 Mpc away, the diffuse IGM contribution to the DM is likely minimal. Nevertheless, we follow the prescription of Simha et al. (2020) to estimate⁶ this contribution at $z = 0.0085$ and find it is $\approx 4 \text{ pc cm}^{-3}$. We conservatively double this value to have a range $\text{DM}_{\text{igm}} \in [0, 8] \text{ pc cm}^{-3}$.

Gas from intervening galaxy halos along the line of sight can contribute to the DM of an observed FRB (e.g., Connor et al. 2023; Lee et al. 2023; Khrykin et al. 2024). Following the methodology used by Simha et al. (2020, 2021, 2023) and Lee et al. (2023), we assume the gas content of galaxy halos extend out to twice their virial radii⁷ and query the NED-LVS for galaxies with impact parameters $b_{\perp} < 1$ Mpc and stellar mass estimates. We then convert the stellar masses for these galaxies into halo masses using a stellar to halo mass ratio (Moster et al. 2013), adopt a modified Navarro-Frenk-White profile (NFW; Navarro et al. 1997) for the halo baryonic gas density, and estimate the resulting DM contribution. The resulting average intervening halo contribution for FRB 20200723B is $\approx 13 \text{ pc cm}^{-3}$. As above, we conservatively double this value to have a range $\text{DM}_{\text{int,halos}} \in [0, 26] \text{ pc cm}^{-3}$.

Taking the minimum contribution of all the above components, we are left with a maximum possible con-

⁶ The code used to estimate DM_{igm} can be found in the FRBs repository at <https://github.com/FRBs/FRB/blob/1eb95e0/frb/dm/igm.py#L341>.

⁷ Free electrons extending to twice the virial radii of galaxies is informed by recent hydrodynamical simulation results (e.g., Ayromlou et al. 2023). For the purposes of our DM budgeting, this assumption also leads to a higher $\text{DM}_{\text{int,halos}}$ upper limit than if we assume gas halos are truncated at the virial radius.

tribution of $\approx 219 \text{ pc cm}^{-3}$ for the combined contribution of DM_{sheet} and DM_{h} . Using the prescription of Simha et al. (2020, 2021, 2023), we find that the halo alone of NGC 4602 could contribute up to $\sim 80 \text{ pc cm}^{-3}$. Given this modeling, NGC 4602 is likely to contribute $\text{DM}_{\text{h}} > 80 \text{ pc cm}^{-3}$ from its total combined halo and ISM contributions. Motivated by these numbers, we assume a minimal host galaxy DM contribution from NGC 4602 of 40 pc cm^{-3} , half the amount from its expected halo contribution alone.⁸ In other words, we obtain $\text{DM}_{\text{h}} \in [40, 219] \text{ pc cm}^{-3}$. Thus, we arrive at a DM contribution range from the W-M sheet of $\text{DM}_{\text{sheet}} \in [0, 179] \text{ pc cm}^{-3}$.

4.3. Column density of the W-M sheet

After the conservative DM budgeting in Section 4.2, we have a plausible range of DM contribution values from the W-M sheet to the total observed DM of FRB 20200723B. The upper limit DM contribution from the filamentary structure is $\text{DM}_{\text{sheet}} < 179 \text{ pc cm}^{-3}$, which is equivalent to a column density $\Sigma < 5.5 \times 10^{20} \text{ cm}^{-2}$. We can compare this column density to gas column densities of filamentary structures found in simulations. The IllustrisTNG project consists of a suite of cosmological magnetohydrodynamical simulations (Pillepich et al. 2018). The three primary simulations are TNG50, TNG100, and TNG300, where the numbers correspond to side length, in Mpc, of the cubic volumes in the simulation box sizes. Figure 2 of Marinacci et al. (2018) show thick slice snapshots from the TNG100 and TNG300 runs. We see a range of column densities $\Sigma = 5 \times 10^{19} \text{ cm}^{-2}$ to $5 \times 10^{20} \text{ cm}^{-2}$ are expected for cosmic filamentary structures, consistent with the column density we find through the W-M sheet.

We can also compare this column density with the stacked Planck y map that Tanimura et al. (2020) made and used to detect the thermal Sunyaev-Zel'dovich (tSZ) signal in filaments. The Compton y parameter quantifies the amplitude of the tSZ signal via the electron pressure integrated along the line of sight,

$$y = \frac{\sigma_T}{m_e c^2} \int k_B n_e T_e dl. \quad (2)$$

Here σ_T is the Thomson cross section, m_e is the electron mass, c is the speed of light, k_B is the Boltzmann constant, n_e is the free electron number density, and T_e is the temperature. From their Figure 5, we take a Compton y parameter at the radial center of a fila-

ment as $y \approx 2 \times 10^{-8}$. If we take our upper limit column density $\int n_e dl < 5.5 \times 10^{20} \text{ cm}^{-2}$ and combine it with this Compton y parameter, then we can estimate a lower limit on the temperature in the W-M sheet to be $T_e > 3 \times 10^5 \text{ K}$. This limit is consistent with the cosmic web filament gas temperature measured by Tanimura et al. (2020) ($\approx 10^6 \text{ K}$).

4.4. Free electron density of the W-M sheet

We also consider the free electron number density. Using the upper limit filamentary DM contribution of 179 pc cm^{-3} , and taking the distance traversed from NGC 4602 through the W-M sheet as $3.9_{-2.6}^{+2.9} \text{ Mpc}$ (Section 4.1), we can set an upper limit on the mean free electron density through the W-M sheet: $\langle n_e \rangle < 4.6_{-2.0}^{+9.6} \times 10^{-5} \text{ cm}^{-3}$. It is of course possible that the medium in the W-M sheet is notably anisotropic, with regions of significant overdensities and underdensities. It is thus also possible that the medium composition in the W-M sheet in front of NGC 4602 (relative to us) significantly differs from the W-M sheet medium behind NGC 4602. Depending on the exact makeup of the W-M sheet, the true free electron constraint could be different. However, the uncertainty in the Tully-Fisher distance to NGC 4602 is large ($\sim 9\%$ relative error), which means the uncertainty in the average sightline free electron density is large. Therefore, we assume that this large uncertainty encompasses any possible medium fluctuations that would affect the free electron density constraint.

To assess the consistency of ΛCDM with our free electron number density limit through the W-M sheet, we can compare that result to $n_{e,0}$, the free electron density of the Universe at $z = 0$. In a fully ionized universe, $n_{e,0}$ is defined as

$$n_{e,0} = f_{d,0} \left(Y_{\text{H}} + \frac{1}{2} Y_{\text{He}} \right) \frac{3H_0^2 \Omega_{b,0}}{8\pi G m_p} \quad (3)$$

where $f_{d,0}$ is the fraction of baryons in diffuse ionized gas at $z = 0$, $\Omega_{b,0}$ is the ΛCDM baryon density parameter at $z = 0$, G is the gravitational constant, m_p is the mass of the proton, H_0 is the Hubble constant, and Y_{H} and Y_{He} are the primordial hydrogen and helium abundances, respectively. Using Planck Collaboration et al. (2020) values, $Y_{\text{H}} + Y_{\text{He}}/2 \approx 0.875$ and $\Omega_{b,0} = 0.04897$. For the fraction of baryons in diffuse ionized gas, we adopt $f_{d,0} = 0.84$ (e.g., Simha et al. 2020; James et al. 2022). With these values, we obtain a free electron den-

⁸ Assuming a minimum $\text{DM}_{\text{h}} = 0 \text{ pc cm}^{-3}$ is less physically motivated and does not qualitatively affect any conclusions.

sity of $n_{e,0} \approx 2 \times 10^{-7} \text{ cm}^{-3}$ for the $z = 0$ Universe.⁹ The upper limit of our free electron density through the W-M sheet is thus no more than ≈ 2 orders of magnitude more overdense than the mean free electron density of the Universe. As one would expect a baryonic structure to be an overdensity, this result can be interpreted as our free electron density upper limit through the W-M sheet being consistent with Λ CDM expectations.

Our free electron density result from FRB 20200723B through the W-M sheet can also be compared to IllustrisTNG simulation results. [Martizzi et al. \(2019\)](#) use snapshots from the TNG100 simulations to study baryons throughout various cosmic web structures at $0 \leq z \leq 8$. They show, in their Figure 4, a phase diagram of baryons at $z = 0$ in filaments and sheets. We see in their results that, for filaments and sheets at $z = 0$, the highest probability density of baryons in the warm-hot intergalactic medium (WHIM, $10^5 \text{ K} < T < 10^7 \text{ K}$), which would dominate in filamentary structures, is around a baryonic number density of $n_{\text{H}} \sim 10^{-6} \text{ cm}^{-3}$ (baryonic number density can be taken as a rough proxy for electron number density, as on large scales, electrons trace baryons). [Galárraga-Espinosa et al. \(2021\)](#) use the TNG300-1 simulation box at $z = 0$ to study gas phases around cosmic filamentary structures. They also find that for the WHIM in filamentary structures, the highest probability density of baryons in the WHIM is just over $n_{\text{H}} \sim 10^{-6} \text{ cm}^{-3}$ (e.g., their Figures 4 and 9). These baryonic number densities of $n_{\text{H}} \sim 10^{-6} \text{ cm}^{-3}$ are consistent with our upper limit $\langle n_e \rangle < 4.6_{-2.0}^{+9.6} \times 10^{-5} \text{ cm}^{-3}$. This average sightline free electron density constraint can also be compared to the analysis done by [Erciyev et al. \(2023\)](#). They use a non-detection of *Planck* tSZ cross-correlations with local Universe galaxies to estimate the average electron pressure; their upper limit on a volume-averaged filament electron number density is higher at $\langle n_e \rangle \lesssim 4 \times 10^{-4} \text{ cm}^{-3}$.

5. SCATTERING TIMESCALE CONSIDERATIONS

The scattering timescale τ of a radio wave, also referred to as the scatter-broadening or pulse broadening time, results from multi-path propagation through inhomogeneities in intervening media. Understanding whether scattering is dominated by the local environment to the FRB (e.g., [Ocker et al. 2023](#)) can give insight into progenitor models. Scattering measurements or limits combined with sightlines through media such as

intervening galaxy halos can provide insights into the gas properties of these environments (e.g., [Prochaska et al. 2019](#); [Connor et al. 2020](#); [Ocker et al. 2021](#)).

For scattering, a frequency-dependent pulse broadening effect can be observed where the resulting one-sided exponential scattering tail follows $\tau \propto \nu^\alpha$. As mentioned in Section 2.2, we adopt $\alpha = -4$, the spectrum predicted by refractive scattering (e.g., [Rickett 1977](#)).

For this section, we adopt a model where the scattering medium is composed of ionized cloudlets embedded within more diffuse gas, a model commonly adopted for the CGM (e.g., [Tumlinson et al. 2017](#)). (In Section 5.1, we discuss another model interpretation as well.) In such a cloudlet model, the degree of fluctuations can be parameterized by the density fluctuation parameter ([Cordes et al. 2016](#))

$$\tilde{F} = \frac{\zeta \epsilon^2}{f_v (l_o^2 l_i)^{1/3}} (\text{pc}^2 \text{ km})^{-1/3} \quad (4)$$

where ζ is the mean density variation between cloudlets, ϵ is the fractional rms of density fluctuations within a cloudlet, f_v is the volume filling factor, and l_o (pc) and l_i (km) define the outer and inner scales of the density fluctuations. A formalism developed by [Cordes et al. \(2016\)](#), [Ocker et al. \(2021\)](#), and [Cordes et al. \(2022\)](#) relates these electron density fluctuations to scattering timescales observed for pulsars and FRBs. This formalism also allows for the geometry of intervening scattering layers boosting the observed scattering timescales via a geometric leverage factor G_{scatt} . For extragalactic distances where the FRB source is at redshift z_s and the intervening scattering layer is at redshift $z_\ell < z_s$, we can define

$$G_{\text{scatt}}(z_s, z_\ell) = \frac{2d_{\text{sl}}d_{\text{lo}}}{Ld_{\text{so}}}. \quad (5)$$

Here, d_{sl} is the angular diameter distance from the source to the layer, d_{lo} is the distance from the layer to the observer, and d_{so} is the distance from the source to the observer. For galaxy disks, the scattering layer thickness can be taken as $L = 1 \text{ kpc}$ ([Cordes et al. 2022](#)). When the scattering layer is in the FRB host galaxy as opposed to an intervening galaxy, the geometric leverage factor is often simplified to $G_{\text{scatt}} = 1$. This simplification comes from $d_{\text{sl}} \rightarrow L/2$ and is thus agnostic as to whether the scattering screen is local ($\sim \text{pc}$) to the FRB as opposed to just within the host galaxy ($\sim \text{kpc}$), as long as the scattering layer thickness is twice the distance from the source to the center of the scattering layer. In practice, however, $G_{\text{scatt}} = 1$ can be a poor approximation — e.g., for pulsars, which reside in the same galaxy as their scattering media, their scattering is dominated by thin, highly localized screens where $L \ll d_{\text{sl}}$ ([Briskin](#)

⁹ Using multiple FRB sightlines, [Khrykin et al. \(2024\)](#) measure the fraction of baryons in the IGM — excluding gas within halos — to be $f_{d,0} = 0.63_{-0.07}^{+0.09}$. This value leads to $n_{e,0} = 4.0_{-0.44}^{+0.57} \times 10^{-8} \text{ cm}^{-3}$.

et al. 2010). While more complicated geometric configurations are not considered in this work, we acknowledge that they are a physical possibility.

In this model, a burst that travels through a layer contributing DM_ℓ (in the rest frame of the scattering medium) with a geometric leverage factor G_{scatt} has an observed scattering time of

$$\tau(\text{DM}_\ell, \nu, z_s, z_\ell) \simeq (48 \text{ ns}) \times A_\tau \nu^{-4} (1 + z_\ell)^{-3} \tilde{F} G_{\text{scatt}}(z_s, z_\ell) \text{DM}_\ell^2 \quad (6)$$

where ν is the observing frequency in GHz (Ocker et al. 2022a). The parameter A_τ parameterizes the shape of the pulse-broadening function; henceforth we adopt $A_\tau = 1$. The derivation of the pre-factor can be found in the Appendix of Cordes et al. (2022). We note that this ionized cloudlet model assumes pulse scatter-broadening is primarily due to diffractive scattering of a volume-filling Kolmogorov spectrum of density fluctuations. However, it is possible that scattering is dominated by refractive scattering due to a small number of intermittent structures with large density variations (Jow et al. 2024). This model assumption should be kept in mind when interpreting subsequent inferences made in this section.

Assuming both FRB 20200723B and its primary scattering screen originate from within NGC 4602 at $z_\ell = 0.0085$, we take the geometric factor to be $G_{\text{scatt}} = 1$. Using Equation 6 and our conservative range of host galaxy DMs (Section 4.2), we can thus constrain the degree of fluctuation in the scattering medium \tilde{F} . We assume the DM contributed by the scattering medium layer is equivalent to the host DM (Cordes et al. 2022). The range of $\text{DM}_h \in [40, 219] \text{ pc cm}^{-3}$ therefore corresponds to a range $\tilde{F} \in [390, 13] (\text{pc}^2 \text{ km})^{-1/3}$, respectively.

It appears that $\tilde{F} \lesssim 1 (\text{pc}^2 \text{ km})^{-1/3}$ for most FRBs for which \tilde{F} is estimated (e.g., Cordes et al. 2022). Additionally, based on Milky Way pulsar observations, the maximum expected \tilde{F} for the thin disk of a spiral galaxy is about $1 (\text{pc}^2 \text{ km})^{-1/3}$ (Ocker et al. 2022a). However, higher \tilde{F} values are possible within the thick disk (Ocker et al. 2021). While FRB 20200723B appears to have an unusually high fluctuation parameter, it is not an infeasible amount when considering Milky Way observations of pulsars. Furthermore, qualitatively, it is possible that there is a high degree of density fluctuations associated with the large observed scattering timescale of FRB 20200723B.

5.1. Can the scattering be explained by the W-M sheet?

Cosmic filamentary structures between galaxy clusters are thought to be composed mostly of $T \gtrsim 10^6 \text{ K}$

gas in the WHIM (e.g., de Graaff et al. 2019; Tanimura et al. 2020; Galárraga-Espinosa et al. 2021). Compared to cooler and denser gas such as, e.g., gas cloudlets in the CGM of galaxies at $T \sim 10^4 \text{ K}$, the WHIM is not thought to significantly contribute to the temporal scattering of radio waves (e.g., Prochaska et al. 2013; Hennawi et al. 2015; Tumlinson et al. 2017; McCourt et al. 2018; Vedantham & Phinney 2019, and references therein). We can verify the plausibility of whether FRB 20200723B can have its large scattering timescale fully explained by passing through an overdensity at the front of the W-M sheet (relative to Earth).

Taking the redshift-independent distance of NGC 4602 and its distance to the front of the W-M sheet, we can derive a geometric factor $G_{\text{scatt}} \approx 6.8 \times 10^3$ (Equation 5). This is the largest possible geometric leverage factor, as it assumes a configuration where all the scattering is attributable to an overdense layer at the furthest possible distance from NGC 4602 while still being in the W-M sheet, thus maximizing the distance from the source to the scattering layer. Considering Equation 4, we note that the volume filling factor of the WHIM can be up to $f_v \sim 0.5$ (Nevalainen et al. 2015) due to its temperature, compared to typical values of $f_v \sim 10^{-3} - 10^{-2}$ for cooler 10^4 K gas commonly invoked to explain scattering (Vedantham & Phinney 2019; Ocker et al. 2021). Using, e.g., a two orders-of-magnitude higher value of f_v to reflect the WHIM in Equation 4, we obtain a two orders-of-magnitude lower \tilde{F} parameter. If we take $\tilde{F} = 10^{-2} (\text{pc}^2 \text{ km})^{-1/3}$ (two orders of magnitude lower than upper range of typical values of \tilde{F} for FRBs; Cordes et al. 2022), the largest possible geometric leverage factor boosting the radio wave scattering in this scenario, and all the possible DM_{sheet} contributing to the scattering, we can obtain a scattering timescale of $\tau_{400 \text{ MHz}} \sim 4 \text{ s}$ from the W-M sheet. While this timescale can be sufficient to explain the observed scattering timescale, any factor of 4 suppression in the relevant parameters — e.g., a lower \tilde{F} parameter, a smaller geometric leverage factor, or a smaller proportion of DM_{sheet} contributing to the scattering, all of which are very possible — means gas from the W-M sheet alone cannot account for the full scattering timescale of FRB 20200723B.

So far we have assumed the cloudlet model discussed at the start of Section 5. However, it is possible that scattering structures within the CGM are better described by a sheet-like geometry, as proposed by Pen & Levin (2014) and Jow et al. (2024) based on observations of pulsar and FRB scintillation. Sheet-like geometries are often invoked to explain why radio sources could exhibit scatter-broadening due to multipath prop-

agation without a large number of images suppressing scintillation (Jow et al. 2024). Edge-on sheets aligned with the line of sight of the FRB would lead to a huge boost in spatial density fluctuations without suppressing FRB scintillation, while also remaining consistent with observations from quasar absorption studies of CGM (Jow et al. 2024). We can consider whether such a sheet-like geometry within the W-M sheet filamentary structure can explain the observed scattering timescale of FRB 20200723B. However, we note that the temperature limit $T_e > 3 \times 10^5$ K we obtained in Section 4.3 for the W-M sheet already suggests that the sheet is unlikely to dominate the scattering, as the high temperature makes it unlikely for matter to clump enough to give the amount of density fluctuations needed for large scatter-broadening timescales.

To assess the plausibility of the scenario where the scattering is dominated by a refractive plasma lens in the W-M sheet, we note that the refractive scattering timescale can be written as (Jow et al. 2024)

$$\tau_{400 \text{ MHz}} = 0.14 \mu\text{S} (1 + z_\ell)^{-3} \times \left(\frac{d_{\text{sl}} d_{\text{lo}} / d_{\text{so}}}{\text{Mpc}} \right) \left(\frac{N_e r}{\text{cm}^{-3}} \right)^2 \left(\frac{f}{\text{MHz}} \right)^{-4} \quad (7)$$

where r is the size of the refractive structure transverse to the line of sight, and for a spherical geometry, $N_e r$ is the effective electron density of the lens. Placing the lens at the furthest edge of the W-M sheet, in order to obtain the observed scattering time, one would require an excess electron density of $n_e \sim 10^3 \text{ cm}^{-3}$. Given our upper-bound on the electron density of the W-M sheet ($\langle n_e \rangle < 4.6_{-2.0}^{+9.6} \times 10^{-5} \text{ cm}^{-3}$), this corresponds to an overdensity a factor of 10^8 larger than the ambient medium. While an inclined sheet-like or filamentary geometry may enhance the effective projected column density, this enhancement is only as large as the aspect ratio, A , of the filament or sheet (the quantity $N_e r$ is at most $n_e A$). Thus, in order to reproduce the observed scattering timescale, the refractive sheet or filament would need to be stretched by at least a factor of 10^8 relative to its thickness — a rather unlikely scenario.

Nonetheless, it would be interesting for future work to consider other models of scattering from media within filamentary structures, particularly one that could explain the large scattering timescale of FRB 20200723B.

5.2. Can the scattering be explained by an unseen true host galaxy lying behind NGC 4602?

Given the combination of high scattering timescale of FRB 20200723B, as well as the much closer distance of NGC 4602 than is naively implied by the total observed extragalactic DM (Section 3), one may ask

whether it is plausible that the FRB originates from a host galaxy *behind* NGC 4602. Setting aside chance alignment probability arguments against the likelihood of such a scenario, we can consider an optimistic scenario where the disk of NGC 4602 is the scattering layer for FRB 20200723B.

Referring to Equations 5 and 6, we see that the combination of fluctuation parameter \tilde{F} , geometric leverage factor G_{scatt} , and DM of the scattering layer DM_ℓ must be consistent with a given scattering timescale. In order to minimize the impact of the geometric leverage factor, we consider an unseen background galaxy only 10 Mpc behind NGC 4602; much further distances are allowed out to z_{max} (e.g., Section 3), but would generally only increase the geometric factor (Equation 5).¹⁰ For similar reasons, we also consider a rather low DM_ℓ contribution of 40 pc cm^{-3} from NGC 4602 (e.g., Section 4.2). In this scenario, such a configuration leads to a geometric leverage factor $G_{\text{scatt}} \approx 1.5 \times 10^4$ and a fluctuation parameter $\tilde{F} \simeq 0.026$ — a not physically implausible value when compared to Milky Way observations of pulsars through the thick disk (e.g., Cordes et al. 2022; Ocker et al. 2022a; Faber et al. 2024). Thus, we have a possible geometric configuration that can reproduce the observed scattering timescale.

However, a putative value $\tilde{F} = 1$ is more likely for the thin disk of a spiral galaxy, and one would expect a much larger DM_ℓ contribution from a sightline through the ISM of a spiral galaxy as massive as NGC 4602. To compare with the Milky Way, the NE2001 model applied at the same Galactic longitude as FRB 20200723B but at a Galactic latitude $b = 15^\circ$ gives a DM of $\sim 135 \text{ pc cm}^{-3}$. As a point of comparison, if we set $\tilde{F} = 1$ and keep the background galaxy at just 10 Mpc behind NGC 4602, we find that a DM_ℓ contribution of $\approx 3.4 \text{ pc cm}^{-3}$ is necessary to obtain the observed scattering timescale, far lower than an expected DM contribution from a sightline through a Milky Way-like Galactic disk, and even through Milky Way-like halos. It is also possible for a background galaxy to lie $\gg 10$ Mpc behind NGC 4602; increasing either G_{scatt} or DM_ℓ any further would lead to a scattering timescale significantly larger than the actual observed scattering timescale of FRB 20200723B.

Thus while in this formalism, the DM and τ measurements of FRB 20200723B alone cannot rule out the possibility of the burst originating from an unseen back-

¹⁰ We argue that given the low DM of FRB 20200723B, a background galaxy with a sightline intersecting the halo of NGC 4602 would likely be visible in archival Legacy Survey imaging. Indeed, in Figure 3, the visible background galaxies have photometric redshifts that place them $\gg 10$ Mpc behind NGC 4602.

ground galaxy and being scattered through the disk of NGC 4602, such a scenario requires a contrived combination of \tilde{F} , DM_ℓ , and chance alignment of a background galaxy.

5.3. Scattering from within NGC 4602

The physically simplest explanation for the scattering timescale of FRB 20200723B is via a scattering layer from within NGC 4602. Bhardwaj et al. (2024) note that there is empirical evidence for a selection bias against FRBs from host galaxies with high inclination angles, and propose large scattering timescales beyond detectability as the cause for this bias, although this correlation remains to be tested with scattering measurements and future studies of telescope systematics. FRB 20200723B, with its high scattering timescale and putative host galaxy NGC 4602, with a high inclination angle $i = 73 \pm 3^\circ$ (Kourkchi et al. 2020), is consistent with the paradigm proposed by Bhardwaj et al. (2024). However, for FRB 20200723B, we caution against over-interpretation from host galaxy inclination angle alone — while highly scattered FRBs may preferentially originate from galaxies with high inclination angles, not every highly scattered FRB *must* originate from one. Some local FRB environments are known to be associated with extreme, dynamic local environments (e.g., Michilli et al. 2018; Ocker et al. 2023); thus, local environments, irrespective of galaxy orientation, could contribute significantly to the scattering timescale. Additionally, not every highly inclined galaxy will emit only highly scattered FRBs. Indeed, FRB 20210603A, a burst localized at detection using VLBI from untargeted observations, is in a galaxy with inclination angle $i = 83 \pm 3^\circ$ and has a significantly smaller scattering timescale at $\tau_{600\text{MHz}} \lesssim 165 \pm 3 \mu\text{s}$ (Cassanelli et al. 2023). Cassanelli et al. (2023) note that their observations and inferred parameters are consistent with FRB 20210603A originating from within its host galaxy disk.

NGC 4602 is a galaxy with a large number of prominent H II regions (Tsvetanov & Petrosian 1995). H II regions are known to contribute to the observed scattering of bursts from pulsars (e.g., Mall et al. 2022; Ocker et al. 2024a,b). For pulsars in the Milky Way, there is an empirical mean scattering–DM relation:

$$\hat{\tau}(\text{DM}, \nu) = (1.9 \times 10^{-7} \text{ ms}) \nu^{-4} \text{DM}^{1.5} \times (1 + 3.55 \times 10^{-5} \text{DM}^{3.0}) \quad (8)$$

where the frequency ν is 1 GHz and $\tau \propto \nu^{-4}$ was adopted as the fiducial scaling to obtain this relation (Cordes et al. 2022). The scatter for this mean relation is $\sigma(\log_{10} \tau) = 0.76$. For FRBs, this $\hat{\tau}(\text{DM}, \nu)$ re-

lation is multiplied by a factor $g_{\text{sw} \rightarrow \text{pw}} = 3$ to account for how scattering from host galaxy interstellar media is larger for FRBs than for Galactic pulsars. This factor is because wavefronts from extragalactic FRBs present as plane waves, while wavefronts from Galactic pulsars are spherical (Cordes et al. 2022). Using this relation and assuming the maximum host DM contribution of $DM_h = 219 \text{ pc cm}^{-3}$, at 1 GHz, FRB 20200723B would still have significant ($\sim 2\sigma$) excess scattering compared to its DM. FRB 20200723B is plotted against the empirical mean–scattering DM relation for FRBs and measurements from Milky Way pulsars in Figure 5.

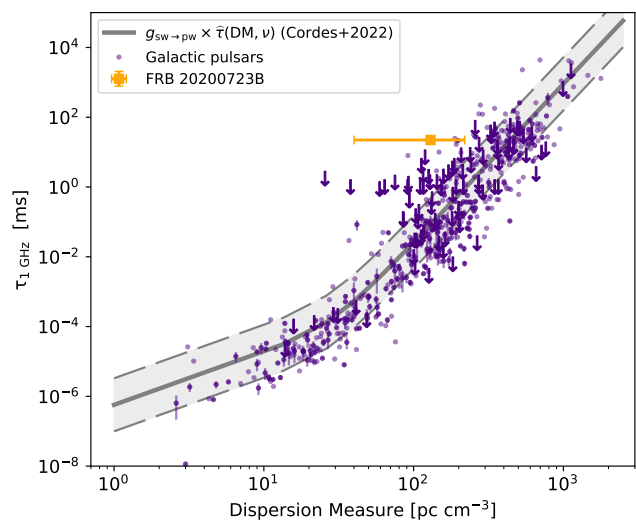


Figure 5. The empirical mean scattering–DM relation (Eqn. 8), multiplied by a factor $g_{\text{sw} \rightarrow \text{pw}} = 3$ to account for scattering for FRBs, is plotted in gray with the $\pm 1\sigma$ region shaded around the line. Scattering and DM data for 570 Galactic pulsars (484 averages, 86 upper limits) are also plotted in indigo; these data are provided courtesy of J. Cordes, and are also published in Cordes et al. (2022). FRB 20200723B is plotted in orange, scaled to its nominal value at 1 GHz using the best-fit scattering timescale and index from Section 2.2; horizontal error bars denote the range of DM contributed by the host galaxy in its rest frame. At the maximum host DM, the observed scattering timescale for FRB 20200723B is $\sim 2\sigma$ greater than what would be expected from this relation (i.e., scattering from a Milky Way-like galaxy). Decreasing the host DM increases the excess of scattering relative to the empirical relation.

However, Ocker et al. (2024a) found that most of ~ 30 identified pulsars with significant excess scattering ($> 2\sigma$), with DMs ranging from tens to hundreds of units, are spatially coincident with ionized foreground struc-

tures such as H II regions.¹¹ It is also worth noting that Ocker et al. (2024a) identified >100 pulsars that intersected H II regions within our Milky Way; thus, qualitatively, it appears to be not uncommon for pulsars to have sightlines that intersect H II regions in inclined galaxies. As such, it is entirely plausible that FRB 20200723B has its high scattering timescale as a result of intersecting an H II region along its line of sight. However, in the absence of a sub-arcsecond localization illuminating the true sightline path of FRB 20200723B, an association with a visible H II region cannot be unambiguously made.

Additionally, while plausible that a foreground H II region is the source of the large scattering timescale of FRB 20200723B, we note there are other Galactic pulsars that lie above the mean scattering–DM relation due to reasons other than foreground H II regions. Such sources include the Crab Pulsar (Staelin & Reifenstein 1968; Deneva et al. 2024; Krishnakumar et al. 2015) and PSR J0540–6919 (Seward et al. 1984), which both lie within supernova remnants, and PSR B1957+20 (Fruchter et al. 1988; Wang et al. 2023; Kuzmin & Losovsky 2007), which is an eclipsing binary pulsar.¹² These pulsars have more local sources of scattering (supernova remnant, binary companion) relative to foreground H II regions. Thus, a broad diversity of physical scenarios are consistent with the observed DM and scattering of FRB 20200723B.

Beyond H II regions, supernova remnants, or eclipsing binary pulsars, the observed scattering timescale could also be explained by an unusually tumultuous circumburst environment, though we note the low RM upper limit found in Section 2.2.3 indicates the circumburst environment is likely not extremely dense and/or strongly magnetized. Future observations and localizations with CHIME/FRB Outriggers (Lanman et al. 2024) will be promising for discovering whether there exist FRBs with high scattering timescales and localizations that coincide with extragalactic H II regions.

5.4. A comparison with injections

In the first CHIME/FRB catalog, CHIME/FRB Collaboration et al. (2021a) noted that CHIME/FRB has

¹¹ For example, Ocker et al. (2024a) present J1730–3350 with a total DM of 261 pc cm⁻³ and scattering timescale $\tau_{1\text{ GHz}} = 27.3$ ms. These values are pleasingly comparable to those of FRB 20200723B, with a maximum host galaxy DM of 219 pc cm⁻³ and scattering timescale $\tau_{1\text{ GHz}} = 22.3$ ms (scaled assuming $\tau \propto \nu^{-4.3}$ from the `fitburst` fit).

¹² Most measurements and references are obtained from the ATNF Pulsar Catalogue at <https://www.atnf.csiro.au/research/pulsar/psrcat/> (Manchester et al. 2005).

a strong observational selection bias against FRBs with a scattering timescale above 10 ms at 600 MHz. This conclusion was reached using the sample of synthetic bursts from an injections campaign in 2020 August, which aimed to characterize which bursts would have been detected as a function of their burst parameters (Merryfield et al. 2023). With such a high scattering timescale, FRB 20200723B should be very difficult for CHIME/FRB to observe, which raises the questions: Why might FRB 20200723B have been detected in the first place, and can we investigate whether FRB 20200723B-like sources are intrinsically rare? We thus aim to use these injections data¹³ to contextualize the detection of FRB 20200723B by CHIME/FRB. In this section, we use the `fitburst` measurements obtained with fixing the scattering index to $\alpha = -4$ (Section 2.2) in order to more properly compare with other CHIME/FRB observations.

Scaled to 600 MHz, the scattering timescale of FRB 20200723B is $\tau_{600\text{ MHz}} \sim 200$ ms, and as noted in Section 2.2, it has a fluence lower limit $\gtrsim 820$ Jy ms. We plot this event, as well as the highly scattered source exhibiting sub-second periodicity FRB 20191221A (with $\tau_{600\text{ MHz}} \sim 340$ ms and fluence $\gtrsim 1200$ Jy ms), against bursts that were injected during the 2020 August injections campaign (Figure 6). We note that both of these bursts have scattering timescales and fluence lower limits larger than those of any burst reported in the first CHIME/FRB catalog, which reported maximum values of $\tau_{600\text{ MHz}} = 0.09 \pm 0.006$ ms and fluence $\gtrsim 95 \pm 41$ Jy ms, respectively (CHIME/FRB Collaboration et al. 2021a).

One thing is immediately clear from Figure 6 — in the fluence–scattering timescale–DM parameter space for bursts injected with a scattering timescale >100 ms at 600 MHz, there are not enough bursts in the injections dataset to fully sample the parameter space. This lack of injected highly scattered bursts is likely due to the “forward-modeling” of determining which bursts to inject, necessary because the injections system lacked the technical capability to inject 5×10^6 synthetic pulses in a timely manner (§4.1.1 in CHIME/FRB Collaboration et al. (2021a)).

While it is plausible that the high fluence of FRB 20200723B was sufficient to overcome the CHIME/FRB detection pipeline selection against highly scattered bursts, a more extensive injections campaign is necessary to better understand how real the fluence–

¹³ The full 2020 August injections data sets, as well as a data usage tutorial, are available at <https://chime-frb-open-data.github.io/>.

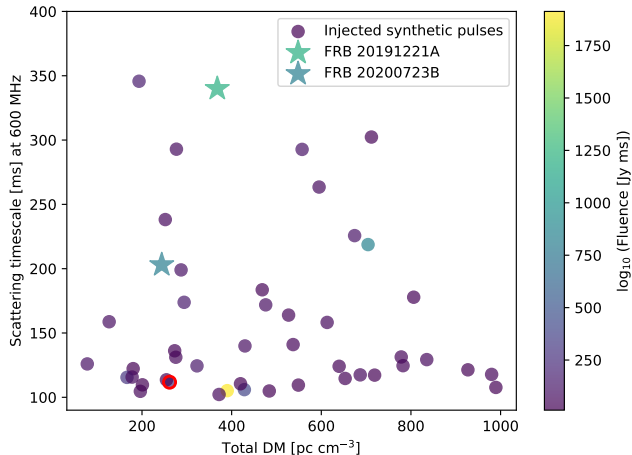


Figure 6. The total DM and scattering timescales of FRB 20191221A and FRB 20200723B, both marked with stars, plotted against the total DM and scattering timescales of bursts from the 2020 August CHIME/FRB injections campaign, plotted as circles. Only bursts injected with a scattering timescale >100 ms are plotted. The marker colors for the injected bursts logarithmically scale with their injected fluence values. For the two real observed FRBs, their marker colors correspond to their fluence lower limit values. The only injections burst detected by the CHIME/FRB detection pipeline is circled in red. There are no injected bursts for which the scattering timescale, fluence, and DM values are comparable to those of FRB 20191221A or FRB 20200723B, greatly limiting our ability to contextualize these observations against CHIME/FRB selection biases.

scattering detection correlation may be, as well as what implications that may have for “scattering horizons” (e.g., Ocker et al. 2022a) for radio transient surveys. To better understand selection biases, it is also necessary for the injections campaign to densely cover a larger parameter space of properties than what was observed. FRB 20200723B also emphasizes the need for a better understanding of selection biases as correlated between burst properties. Accordingly, a more thorough injections campaign is planned for the second CHIME/FRB catalog.

6. DISCUSSION & CONCLUSION

The most probable association of FRB 20200723B to a putative local Universe host galaxy, NGC 4602, has allowed us to explore its sightline properties. We find that this FRB passes through the “W-M sheet”, a filamentary structure associated with the Virgo Cluster (Kim et al. 2016). Budgeting the total DM along the line of sight, we can constrain the average column density along the line of sight of this sheet to be $\Sigma < 5.5 \times 10^{20} \text{ cm}^{-2}$, consistent with gas density results from IllustrisTNG. We also combine this result with Compton y values cor-

responding to filaments to obtain a lower limit on the average temperature in the W-M sheet, $T > 3 \times 10^5 \text{ K}$. While a filament is structurally distinct from a sheet, and thus this temperature limit is perhaps not the most accurate or constraining, one can imagine improved constraints in the near future for specific filaments and sheets with updated tSZ observations of sheets and better-localized FRBs in the local Universe. We can also very conservatively constrain the average free electron density along the line of sight of this sheet to be $\langle n_e \rangle < 4.6^{+9.6}_{-2.0} \times 10^{-5} \text{ cm}^{-3}$, where the main source of uncertainty is the redshift-independent distance measurement of NGC 4602. This free electron density constraint is also in broad agreement with simulations.

We note this free electron density upper limit corresponds to a filamentary DM contribution of $\text{DM}_{\text{sheet}} \sim 179 \text{ pc cm}^{-3}$, over 70% of the total observed DM of $\sim 244 \text{ pc cm}^{-3}$ of FRB 20200723B. While Walker et al. (2024) find in simulations that filamentary contributions to DM dominate starting from $z = 0.1$ (the non-zero redshift snapshot they consider), it has not been standard to attribute so large a percentage of DM of FRBs to the intervening cosmic web.

With this DM budgeting, using formalism developed by Cordes et al. (2016), Ocker et al. (2021), and Cordes et al. (2022) for scattering from ionized cloudlets, we find that the large scattering timescale of FRB 20200723B is reasonably attributable to its host galaxy. Adopting a model where there are cloudlets that could cause radio-wave scattering within the warm-hot intergalactic medium dominating galaxy cluster filaments, we find that FRB 20200723B is unlikely to have its scattering due to the filamentary structure it resides within, as the physical configurations required are rather fine-tuned. We also posit that this FRB, despite its high scattering timescale, is unlikely to originate from an unseen background galaxy behind the disk of NGC 4602, in large part due to chance alignment probabilities. More precise localizations (e.g., sub-arcsecond instead of \sim arcminute) would provide clarity on such a scenario.

We compare the DM and scattering measurements of FRB 20200723B with those of pulsars compiled by Ocker et al. (2024a), and find it physically plausible that if the scattering layer of FRB 20200723B is within its host galaxy, it may be a result of intersecting an H II region within NGC 4602 along its sightline. Such an intersection probability is increased by the high inclination angle of NGC 4602. The scattering excess compared to the mean scattering–DM relation is comparable to the scattering excess of pulsars found to be associated with foreground ionized structures; many more pulsars have also been identified to have sightlines through fore-

ground H II regions (Ocker et al. 2024a). Although rarer, scattering due to supernova remnants or eclipsing materials have also been observed for Milky Way pulsars at levels comparable to the scattering excess seen for FRB 20200723B. We find a sightline intersection with an H II region within the host galaxy to be a more natural explanation for the large scattering timescale of FRB 20200723B, compared to requiring an improbable (though not impossible) alignment of physical parameters to explain the scattering if it were attributable to the W-M sheet (Section 5.1), or to a scenario where the unseen true host galaxy lies behind NGC 4602 (Section 5.2). We also note that the more DM we attribute to a screen within the host galaxy of NGC 4602, the less the observed scattering is in excess of the empirical mean scattering–DM relation, and also the less DM is attributable to the filamentary structure, thus making the free electron density constraints tighter for the W-M sheet.

In over five years of operation, CHIME/FRB has seen only two bursts with scattering timescales $\tau_{400\text{ MHz}} > 1$ second: FRB 20191221A and FRB 20200723B. That we even see FRBs with such high scattering timescales is surprising, given that CHIME/FRB Collaboration et al. (2021a) have noted that CHIME/FRB has an extreme observation selection bias against bursts with scattering timescales $\tau_{600\text{ MHz}} > 10$ ms. What both FRB 20200723B and FRB 20191221A have in common is high burst fluences, suggesting that the selection against large scattering can be overcome with sufficiently bright bursts. However, the parameter space explored by injections for high fluence-high scattering bursts is sparse. Thus, until a more comprehensive injections campaign is done, there is no way to quantify whether these high fluence-high scattering bursts are intrinsically rare, or just observationally selected against by CHIME/FRB.

FRB 20200723B already demonstrates the ability of FRBs to sensitively probe ionized media along their sightlines using both their DM and their scattering properties. We note that local Universe FRBs hold especially promising sightline constraints given the amount of detailed DM budgeting that it is possible to do. Bursts such as FRB 20200723B, but with a full baseband capture for polarimetric information, can reveal even more information about the interplay between fluence, scattering timescale, and local magneto-ionospheric environment for FRBs. As FRB 20200723B was detected before any CHIME/FRB Outriggers stations came online, only an \sim arcminute-scale localization was possible; with sub-arcsecond localizations, observations of FRB 20200723B-like sources could start to further probe

possible CGM substructure of other galaxies (e.g., Faber et al. 2024). With the rapidly growing sample of FRBs, studies of their propagation effects will be a powerful probe of the Universe.

We acknowledge that CHIME is located on the traditional, ancestral, and unceded territory of the Syilx/Okanagan people. We are grateful to the staff of the Dominion Radio Astrophysical Observatory, which is operated by the National Research Council of Canada. CHIME is funded by a grant from the Canada Foundation for Innovation (CFI) 2012 Leading Edge Fund (Project 31170) and by contributions from the provinces of British Columbia, Québec and Ontario. The CHIME/FRB Project is funded by a grant from the CFI 2015 Innovation Fund (Project 33213) and by contributions from the provinces of British Columbia and Québec, and by the Dunlap Institute for Astronomy and Astrophysics at the University of Toronto. Additional support was provided by the Canadian Institute for Advanced Research (CIFAR), the Trottier Space Institute at McGill University, and the University of British Columbia.

The authors would like to thank Jim Cordes for kindly providing pulsar data.

A.B.P. is a Banting Fellow, a McGill Space Institute (MSI) Fellow, and a Fonds de Recherche du Québec – Nature et Technologies (FRQNT) postdoctoral fellow. A.M.C. is funded by an NSERC Doctoral Postgraduate Scholarship. A.P. is funded by the NSERC Canada Graduate Scholarships – Doctoral program. B. C. A. is supported by an FRQNT Doctoral Research Award. C. L. is supported by NASA through the NASA Hubble Fellowship grant HST-HF2-51536.001-A awarded by the Space Telescope Science Institute, which is operated by the Association of Universities for Research in Astronomy, Inc., under NASA contract NAS5-26555. FRB research at UBC is supported by an NSERC Discovery Grant and by the Canadian Institute for Advanced Research. The baseband recording system on CHIME/FRB is funded in part by a CFI John R. Evans Leaders Fund grant to I.H.S. J.X.P., L.K., L.M., and S.S. acknowledge support from NSF grants AST-1911140, AST-1910471, and AST-2206490 as members of the Fast and Fortunate for FRB Follow-up team. K.N. is an MIT Kavli Fellow. K.R.S. is supported by FRQNT doctoral research award. K.S. is supported by the NSF Graduate Research Fellowship Program. K.W.M. holds the Adam J. Burgasser Chair in Astrophysics and is supported by the Carl G. and Shirley Sontheimer Research Fund. M.B. is a McWilliams fellow and an International

Astronomical Union Gruber fellow. M.B. also receives support from the McWilliams seed grant. M.W.S. acknowledges support from the Trottier Space Institute Fellowship program. S.S. is a Northwestern University and University of Chicago Brinson Postdoctoral Fellow. V.M.K. holds the Lorne Trottier Chair in Astrophysics & Cosmology, a Distinguished James McGill Professorship, and receives support from an NSERC Discovery grant (RGPIN 228738-13), from an R. Howard Webster Foundation Fellowship from CIFAR. Z.P. is supported by an NWO Veni fellowship (VI.Veni.222.295).

Facility: CHIME

Software: APLpy (Robitaille & Bressert 2012; Robitaille 2019), astropath (Aggarwal et al. 2021), astropy (Astropy Collaboration et al. 2013, 2018, 2022), fitburst (Fonseca et al. 2024), matplotlib (Hunter 2007), NE2001p (Ocker & Cordes 2024), numpy (Harris et al. 2020), PyGEDM (Price et al. 2021), reproject (Robitaille et al. 2020), RM-CLEAN (Heald et al. 2009), RM-synthesis (Brentjens & de Bruyn 2005), RM-tools (Purcell et al. 2020), scipy (Virtanen et al. 2020)

REFERENCES

- Aggarwal, K., Budavári, T., Deller, A. T., et al. 2021, *ApJ*, 911, 95, doi: [10.3847/1538-4357/abe8d2](https://doi.org/10.3847/1538-4357/abe8d2)
- Andersen, B. C., Patel, C., Brar, C., et al. 2023, *AJ*, 166, 138, doi: [10.3847/1538-3881/accc78](https://doi.org/10.3847/1538-3881/accc78)
- Anna-Thomas, R., Connor, L., Dai, S., et al. 2023, *Science*, 380, 599, doi: [10.1126/science.abo6526](https://doi.org/10.1126/science.abo6526)
- Astropy Collaboration, Robitaille, T. P., Tollerud, E. J., et al. 2013, *A&A*, 558, A33, doi: [10.1051/0004-6361/201322068](https://doi.org/10.1051/0004-6361/201322068)
- Astropy Collaboration, Price-Whelan, A. M., Sipőcz, B. M., et al. 2018, *AJ*, 156, 123, doi: [10.3847/1538-3881/aabc4f](https://doi.org/10.3847/1538-3881/aabc4f)
- Astropy Collaboration, Price-Whelan, A. M., Lim, P. L., et al. 2022, *ApJ*, 935, 167, doi: [10.3847/1538-4357/ac7c74](https://doi.org/10.3847/1538-4357/ac7c74)
- Ayromlou, M., Nelson, D., & Pillepich, A. 2023, *MNRAS*, 524, 5391, doi: [10.1093/mnras/stad2046](https://doi.org/10.1093/mnras/stad2046)
- Bhardwaj, M., Lee, J., & Ji, K. 2024, arXiv e-prints, arXiv:2408.01876, doi: [10.48550/arXiv.2408.01876](https://doi.org/10.48550/arXiv.2408.01876)
- Bhardwaj, M., Gaensler, B. M., Kaspi, V. M., et al. 2021a, *ApJL*, 910, L18, doi: [10.3847/2041-8213/abeaa6](https://doi.org/10.3847/2041-8213/abeaa6)
- Bhardwaj, M., Kirichenko, A. Y., Michilli, D., et al. 2021b, *ApJL*, 919, L24, doi: [10.3847/2041-8213/ac223b](https://doi.org/10.3847/2041-8213/ac223b)
- Bond, J. R., Kofman, L., & Pogosyan, D. 1996, *Nature*, 380, 603, doi: [10.1038/380603a0](https://doi.org/10.1038/380603a0)
- Brentjens, M. A., & de Bruyn, A. G. 2005, *A&A*, 441, 1217, doi: [10.1051/0004-6361:20052990](https://doi.org/10.1051/0004-6361:20052990)
- Brisken, W. F., Macquart, J. P., Gao, J. J., et al. 2010, *ApJ*, 708, 232, doi: [10.1088/0004-637X/708/1/232](https://doi.org/10.1088/0004-637X/708/1/232)
- Burn, B. J. 1966, *MNRAS*, 133, 67, doi: [10.1093/mnras/133.1.67](https://doi.org/10.1093/mnras/133.1.67)
- Cassanelli, T., Leung, C., Sanghavi, P., et al. 2023, arXiv e-prints, arXiv:2307.09502, doi: [10.48550/arXiv.2307.09502](https://doi.org/10.48550/arXiv.2307.09502)
- Castignani, G., Vulcani, B., Finn, R. A., et al. 2022, *ApJS*, 259, 43, doi: [10.3847/1538-4365/ac45f7](https://doi.org/10.3847/1538-4365/ac45f7)
- Cen, R., & Ostriker, J. P. 2006, *ApJ*, 650, 560, doi: [10.1086/506505](https://doi.org/10.1086/506505)
- CHIME Collaboration, Amiri, M., Bandura, K., et al. 2022, *ApJS*, 261, 29, doi: [10.3847/1538-4365/ac6fd9](https://doi.org/10.3847/1538-4365/ac6fd9)
- CHIME/FRB Collaboration, Amiri, M., Bandura, K., et al. 2018, *ApJ*, 863, 48, doi: [10.3847/1538-4357/aad188](https://doi.org/10.3847/1538-4357/aad188)
- CHIME/FRB Collaboration, Amiri, M., Andersen, B. C., et al. 2021a, *ApJS*, 257, 59, doi: [10.3847/1538-4365/ac33ab](https://doi.org/10.3847/1538-4365/ac33ab)
- CHIME/FRB Collaboration, Andersen, B. C., Bandura, K., et al. 2021b, arXiv e-prints, arXiv:2107.08463, <https://arxiv.org/abs/2107.08463>
- CHIME/FRB Collaboration, Amiri, M., Andersen, B. C., et al. 2024, *ApJ*, 969, 145, doi: [10.3847/1538-4357/ad464b](https://doi.org/10.3847/1538-4357/ad464b)
- Connor, L., van Leeuwen, J., Oostrum, L. C., et al. 2020, *MNRAS*, 499, 4716, doi: [10.1093/mnras/staa3009](https://doi.org/10.1093/mnras/staa3009)
- Connor, L., Ravi, V., Catha, M., et al. 2023, *ApJL*, 949, L26, doi: [10.3847/2041-8213/acd3ea](https://doi.org/10.3847/2041-8213/acd3ea)
- Connor, L., Ravi, V., Sharma, K., et al. 2024, arXiv e-prints, arXiv:2409.16952, doi: [10.48550/arXiv.2409.16952](https://doi.org/10.48550/arXiv.2409.16952)
- Cook, A. M., Bhardwaj, M., Gaensler, B. M., et al. 2023a, *ApJ*, 946, 58, doi: [10.3847/1538-4357/acbbd0](https://doi.org/10.3847/1538-4357/acbbd0)
- Cook, D. O., Mazzarella, J. M., Helou, G., et al. 2023b, *ApJS*, 268, 14, doi: [10.3847/1538-4365/acdd06](https://doi.org/10.3847/1538-4365/acdd06)
- Cordes, J. M., & Lazio, T. J. W. 2002, arXiv e-prints, astro. <https://arxiv.org/abs/astro-ph/0207156>
- Cordes, J. M., Ocker, S. K., & Chatterjee, S. 2022, *ApJ*, 931, 88, doi: [10.3847/1538-4357/ac6873](https://doi.org/10.3847/1538-4357/ac6873)
- Cordes, J. M., Wharton, R. S., Spitler, L. G., Chatterjee, S., & Wasserman, I. 2016, arXiv e-prints, arXiv:1605.05890, doi: [10.48550/arXiv.1605.05890](https://doi.org/10.48550/arXiv.1605.05890)
- de Graaff, A., Cai, Y.-C., Heymans, C., & Peacock, J. A. 2019, *A&A*, 624, A48, doi: [10.1051/0004-6361/201935159](https://doi.org/10.1051/0004-6361/201935159)
- de Vaucouleurs, G. 1971, *PASP*, 83, 113, doi: [10.1086/129088](https://doi.org/10.1086/129088)
- Deneva, J. S., McLaughlin, M., Olszanski, T. E. E., et al. 2024, *ApJS*, 271, 23, doi: [10.3847/1538-4365/ad19da](https://doi.org/10.3847/1538-4365/ad19da)

- Dey, A., Schlegel, D. J., Lang, D., et al. 2019, *AJ*, 157, 168, doi: [10.3847/1538-3881/ab089d](https://doi.org/10.3847/1538-3881/ab089d)
- Dolag, K., Gaensler, B. M., Beck, A. M., & Beck, M. C. 2015, *MNRAS*, 451, 4277, doi: [10.1093/mnras/stv1190](https://doi.org/10.1093/mnras/stv1190)
- Eckert, D., Jauzac, M., Shan, H., et al. 2015, *Nature*, 528, 105, doi: [10.1038/nature16058](https://doi.org/10.1038/nature16058)
- Erciyes, C., Basu, K., Kim, S., & Rey, S.-C. 2023, *A&A*, 675, A63, doi: [10.1051/0004-6361/202245187](https://doi.org/10.1051/0004-6361/202245187)
- Faber, J. T., Ravi, V., Ocker, S. K., et al. 2024, arXiv e-prints, arXiv:2405.14182, doi: [10.48550/arXiv.2405.14182](https://doi.org/10.48550/arXiv.2405.14182)
- Feltre, A., Gruppioni, C., Marchetti, L., et al. 2023, *A&A*, 675, A74, doi: [10.1051/0004-6361/202245516](https://doi.org/10.1051/0004-6361/202245516)
- Feng, Y., Li, D., Yang, Y.-P., et al. 2022, *Science*, 375, 1266, doi: [10.1126/science.abl7759](https://doi.org/10.1126/science.abl7759)
- Fonseca, E., Pleunis, Z., Breitman, D., et al. 2024, *ApJS*, 271, 49, doi: [10.3847/1538-4365/ad27d6](https://doi.org/10.3847/1538-4365/ad27d6)
- Fruchter, A. S., Stinebring, D. R., & Taylor, J. H. 1988, *Nature*, 333, 237, doi: [10.1038/333237a0](https://doi.org/10.1038/333237a0)
- Galárraga-Espinosa, D., Aghanim, N., Langer, M., & Tanimura, H. 2021, *A&A*, 649, A117, doi: [10.1051/0004-6361/202039781](https://doi.org/10.1051/0004-6361/202039781)
- Harris, C. R., Millman, K. J., van der Walt, S. J., et al. 2020, *Nature*, 585, 357, doi: [10.1038/s41586-020-2649-2](https://doi.org/10.1038/s41586-020-2649-2)
- Heald, G., Braun, R., & Edmonds, R. 2009, *A&A*, 503, 409, doi: [10.1051/0004-6361/200912240](https://doi.org/10.1051/0004-6361/200912240)
- Hennawi, J. F., Prochaska, J. X., Cantalupo, S., & Arrigoni-Battaia, F. 2015, *Science*, 348, 779, doi: [10.1126/science.aaa5397](https://doi.org/10.1126/science.aaa5397)
- Hunter, J. D. 2007, *Computing in Science and Engineering*, 9, 90, doi: [10.1109/MCSE.2007.55](https://doi.org/10.1109/MCSE.2007.55)
- Hutschenreuter, S., Anderson, C. S., Betti, S., et al. 2022, *A&A*, 657, A43, doi: [10.1051/0004-6361/202140486](https://doi.org/10.1051/0004-6361/202140486)
- Ibik, A. L., Drout, M. R., Gaensler, B. M., et al. 2024, *ApJ*, 961, 99, doi: [10.3847/1538-4357/ad0893](https://doi.org/10.3847/1538-4357/ad0893)
- James, C. W. 2023, *PASA*, 40, e057, doi: [10.1017/pasa.2023.51](https://doi.org/10.1017/pasa.2023.51)
- James, C. W., Ghosh, E. M., Prochaska, J. X., et al. 2022, *MNRAS*, 516, 4862, doi: [10.1093/mnras/stac2524](https://doi.org/10.1093/mnras/stac2524)
- Jow, D. L., Wu, X., & Pen, U.-L. 2024, *Proceedings of the National Academy of Sciences*, 121, e2406783121, doi: [10.1073/pnas.2406783121](https://doi.org/10.1073/pnas.2406783121)
- Keating, L. C., & Pen, U.-L. 2020, *MNRAS*, 496, L106, doi: [10.1093/mnrasl/slaa095](https://doi.org/10.1093/mnrasl/slaa095)
- Khrykin, I. S., Ata, M., Lee, K.-G., et al. 2024, arXiv e-prints, arXiv:2402.00505, doi: [10.48550/arXiv.2402.00505](https://doi.org/10.48550/arXiv.2402.00505)
- Kim, S., Rey, S.-C., Bureau, M., et al. 2016, *ApJ*, 833, 207, doi: [10.3847/1538-4357/833/2/207](https://doi.org/10.3847/1538-4357/833/2/207)
- Kirsten, F., Marcote, B., Nimmo, K., et al. 2022, *Nature*, 602, 585, doi: [10.1038/s41586-021-04354-w](https://doi.org/10.1038/s41586-021-04354-w)
- Kourkchi, E., Tully, R. B., Eftekhazadeh, S., et al. 2020, *ApJ*, 902, 145, doi: [10.3847/1538-4357/abb66b](https://doi.org/10.3847/1538-4357/abb66b)
- Krishnakumar, M. A., Joshi, B. C., & Manoharan, P. K. 2017, *ApJ*, 846, 104, doi: [10.3847/1538-4357/aa7af2](https://doi.org/10.3847/1538-4357/aa7af2)
- Krishnakumar, M. A., Mitra, D., Naidu, A., Joshi, B. C., & Manoharan, P. K. 2015, *ApJ*, 804, 23, doi: [10.1088/0004-637X/804/1/23](https://doi.org/10.1088/0004-637X/804/1/23)
- Kuzmin, A. D., & Losovsky, B. Y. 2007, *Astronomical and Astrophysical Transactions*, 26, 597, doi: [10.1080/10556790701610282](https://doi.org/10.1080/10556790701610282)
- Lanman, A. E., Andrew, S., Lazda, M., et al. 2024, *AJ*, 168, 87, doi: [10.3847/1538-3881/ad5838](https://doi.org/10.3847/1538-3881/ad5838)
- Lee, K.-G., Khrykin, I. S., Simha, S., et al. 2023, *ApJL*, 954, L7, doi: [10.3847/2041-8213/acefb5](https://doi.org/10.3847/2041-8213/acefb5)
- Lorimer, D. R., Bailes, M., McLaughlin, M. A., Narkevic, D. J., & Crawford, F. 2007, *Science*, 318, 777, doi: [10.1126/science.1147532](https://doi.org/10.1126/science.1147532)
- Lorimer, D. R., & Kramer, M. 2012, *Handbook of Pulsar Astronomy*
- Mall, G., Main, R. A., Antoniadis, J., et al. 2022, *MNRAS*, 511, 1104, doi: [10.1093/mnras/stac096](https://doi.org/10.1093/mnras/stac096)
- Manchester, R. N., Hobbs, G. B., Teoh, A., & Hobbs, M. 2005, *AJ*, 129, 1993, doi: [10.1086/428488](https://doi.org/10.1086/428488)
- Marinacci, F., Vogelsberger, M., Pakmor, R., et al. 2018, *MNRAS*, 480, 5113, doi: [10.1093/mnras/sty2206](https://doi.org/10.1093/mnras/sty2206)
- Martizzi, D., Vogelsberger, M., Artale, M. C., et al. 2019, *MNRAS*, 486, 3766, doi: [10.1093/mnras/stz1106](https://doi.org/10.1093/mnras/stz1106)
- Masui, K., Lin, H.-H., Sievers, J., et al. 2015, *Nature*, 528, 523, doi: [10.1038/nature15769](https://doi.org/10.1038/nature15769)
- McCourt, M., Oh, S. P., O'Leary, R., & Madigan, A.-M. 2018, *MNRAS*, 473, 5407, doi: [10.1093/mnras/stx2687](https://doi.org/10.1093/mnras/stx2687)
- Mckinven, R., Michilli, D., Masui, K., et al. 2021, *ApJ*, 920, 138, doi: [10.3847/1538-4357/ac126a](https://doi.org/10.3847/1538-4357/ac126a)
- Mckinven, R., Gaensler, B. M., Michilli, D., et al. 2023, *ApJ*, 950, 12, doi: [10.3847/1538-4357/acc65f](https://doi.org/10.3847/1538-4357/acc65f)
- Merryfield, M., Tendulkar, S. P., Shin, K., et al. 2023, *AJ*, 165, 152, doi: [10.3847/1538-3881/ac9ab5](https://doi.org/10.3847/1538-3881/ac9ab5)
- Meyer, M. J., Zwaan, M. A., Webster, R. L., et al. 2004, *MNRAS*, 350, 1195, doi: [10.1111/j.1365-2966.2004.07710.x](https://doi.org/10.1111/j.1365-2966.2004.07710.x)
- Michilli, D., Seymour, A., Hessels, J. W. T., et al. 2018, *Nature*, 553, 182, doi: [10.1038/nature25149](https://doi.org/10.1038/nature25149)
- Michilli, D., Masui, K. W., Mckinven, R., et al. 2021, *ApJ*, 910, 147, doi: [10.3847/1538-4357/abe626](https://doi.org/10.3847/1538-4357/abe626)
- Moster, B. P., Naab, T., & White, S. D. M. 2013, *MNRAS*, 428, 3121, doi: [10.1093/mnras/sts261](https://doi.org/10.1093/mnras/sts261)
- Navarro, J. F., Frenk, C. S., & White, S. D. M. 1997, *ApJ*, 490, 493, doi: [10.1086/304888](https://doi.org/10.1086/304888)

- Nevalainen, J., Tempel, E., Liivamägi, L. J., et al. 2015, *A&A*, 583, A142, doi: [10.1051/0004-6361/201526443](https://doi.org/10.1051/0004-6361/201526443)
- Ng, C., Vanderlinde, K., Paradise, A., et al. 2017, in XXXII International Union of Radio Science General Assembly & Scientific Symposium (URSI GASS) 2017, 4, doi: [10.23919/URSIGASS.2017.8105318](https://doi.org/10.23919/URSIGASS.2017.8105318)
- Nicastro, F., Kaastra, J., Krongold, Y., et al. 2018, *Nature*, 558, 406, doi: [10.1038/s41586-018-0204-1](https://doi.org/10.1038/s41586-018-0204-1)
- Nimmo, K., Pleunis, Z., Beniamini, P., et al. 2024, arXiv e-prints, arXiv:2406.11053, doi: [10.48550/arXiv.2406.11053](https://doi.org/10.48550/arXiv.2406.11053)
- Ocker, S. K., Anderson, L. D., Lazio, T. J. W., Cordes, J. M., & Ravi, V. 2024a, arXiv e-prints, arXiv:2406.07664, doi: [10.48550/arXiv.2406.07664](https://doi.org/10.48550/arXiv.2406.07664)
- Ocker, S. K., & Cordes, J. M. 2024, *Research Notes of the American Astronomical Society*, 8, 17, doi: [10.3847/2515-5172/ad1bfl](https://doi.org/10.3847/2515-5172/ad1bfl)
- Ocker, S. K., Cordes, J. M., & Chatterjee, S. 2021, *ApJ*, 911, 102, doi: [10.3847/1538-4357/abeb6e](https://doi.org/10.3847/1538-4357/abeb6e)
- Ocker, S. K., Cordes, J. M., Chatterjee, S., & Gorsuch, M. R. 2022a, *ApJ*, 934, 71, doi: [10.3847/1538-4357/ac75ba](https://doi.org/10.3847/1538-4357/ac75ba)
- Ocker, S. K., Cordes, J. M., Chatterjee, S., et al. 2023, *MNRAS*, 519, 821, doi: [10.1093/mnras/stac3547](https://doi.org/10.1093/mnras/stac3547)
- . 2022b, *ApJ*, 931, 87, doi: [10.3847/1538-4357/ac6504](https://doi.org/10.3847/1538-4357/ac6504)
- . 2024b, *MNRAS*, 527, 7568, doi: [10.1093/mnras/stad3683](https://doi.org/10.1093/mnras/stad3683)
- Pandhi, A., Pleunis, Z., Mckinven, R., et al. 2024, *ApJ*, 968, 50, doi: [10.3847/1538-4357/ad40aa](https://doi.org/10.3847/1538-4357/ad40aa)
- Peebles, P. J. E. 2022, *Annals of Physics*, 447, 169159, doi: [10.1016/j.aop.2022.169159](https://doi.org/10.1016/j.aop.2022.169159)
- Pen, U.-L., & Levin, Y. 2014, *MNRAS*, 442, 3338, doi: [10.1093/mnras/stu1020](https://doi.org/10.1093/mnras/stu1020)
- Pillepich, A., Springel, V., Nelson, D., et al. 2018, *MNRAS*, 473, 4077, doi: [10.1093/mnras/stx2656](https://doi.org/10.1093/mnras/stx2656)
- Planck Collaboration, Aghanim, N., Akrami, Y., et al. 2020, *A&A*, 641, A6, doi: [10.1051/0004-6361/201833910](https://doi.org/10.1051/0004-6361/201833910)
- Price, D. C., Flynn, C., & Deller, A. 2021, *PASA*, 38, e038, doi: [10.1017/pasa.2021.33](https://doi.org/10.1017/pasa.2021.33)
- Prochaska, J. X., Hennawi, J. F., & Simcoe, R. A. 2013, *ApJL*, 762, L19, doi: [10.1088/2041-8205/762/2/L19](https://doi.org/10.1088/2041-8205/762/2/L19)
- Prochaska, J. X., & Zheng, Y. 2019, *MNRAS*, 485, 648, doi: [10.1093/mnras/stz261](https://doi.org/10.1093/mnras/stz261)
- Prochaska, J. X., Macquart, J.-P., McQuinn, M., et al. 2019, *Science*, 366, 231, doi: [10.1126/science.aay0073](https://doi.org/10.1126/science.aay0073)
- Purcell, C. R., Van Eck, C. L., West, J., Sun, X. H., & Gaensler, B. M. 2020, *ASCL*, 2005.003. <http://ascl.net/2005.003>
- Reiprich, T. H., Basu, K., Etti, S., et al. 2013, *SSRv*, 177, 195, doi: [10.1007/s11214-013-9983-8](https://doi.org/10.1007/s11214-013-9983-8)
- Rickett, B., Johnston, S., Tomlinson, T., & Reynolds, J. 2009, *MNRAS*, 395, 1391, doi: [10.1111/j.1365-2966.2009.14471.x](https://doi.org/10.1111/j.1365-2966.2009.14471.x)
- Rickett, B. J. 1977, *ARA&A*, 15, 479, doi: [10.1146/annurev.aa.15.090177.002403](https://doi.org/10.1146/annurev.aa.15.090177.002403)
- Robitaille, T. 2019, *APLpy v2.0: The Astronomical Plotting Library in Python*, doi: [10.5281/zenodo.2567476](https://doi.org/10.5281/zenodo.2567476)
- Robitaille, T., & Bressert, E. 2012, *APLpy: Astronomical Plotting Library in Python*, *Astrophysics Source Code Library*. <http://ascl.net/1208.017>
- Robitaille, T., Deil, C., & Ginsburg, A. 2020, reproject: Python-based astronomical image reprojection, *Astrophysics Source Code Library*, record ascl:2011.023
- Sammons, M. W., Deller, A. T., Glowacki, M., et al. 2023, *MNRAS*, 525, 5653, doi: [10.1093/mnras/stad2631](https://doi.org/10.1093/mnras/stad2631)
- Schoen, E., Leung, C., Masui, K., et al. 2021, *Research Notes of the American Astronomical Society*, 5, 271, doi: [10.3847/2515-5172/ac3af9](https://doi.org/10.3847/2515-5172/ac3af9)
- Seward, F. D., Harnden, F. R., J., & Helfand, D. J. 1984, *ApJL*, 287, L19, doi: [10.1086/184388](https://doi.org/10.1086/184388)
- Shin, K., Masui, K. W., Bhardwaj, M., et al. 2023, *ApJ*, 944, 105, doi: [10.3847/1538-4357/acaf06](https://doi.org/10.3847/1538-4357/acaf06)
- Simha, S., Burchett, J. N., Prochaska, J. X., et al. 2020, *ApJ*, 901, 134, doi: [10.3847/1538-4357/abafc3](https://doi.org/10.3847/1538-4357/abafc3)
- Simha, S., Tejos, N., Prochaska, J. X., et al. 2021, *ApJ*, 921, 134, doi: [10.3847/1538-4357/ac2000](https://doi.org/10.3847/1538-4357/ac2000)
- Simha, S., Lee, K.-G., Prochaska, J. X., et al. 2023, *ApJ*, 954, 71, doi: [10.3847/1538-4357/ace324](https://doi.org/10.3847/1538-4357/ace324)
- Staelin, D. H., & Reifenstein, Edward C., I. 1968, *Science*, 162, 1481, doi: [10.1126/science.162.3861.1481](https://doi.org/10.1126/science.162.3861.1481)
- Steer, I., Madore, B. F., Mazzarella, J. M., et al. 2017, *AJ*, 153, 37, doi: [10.3847/1538-3881/153/1/37](https://doi.org/10.3847/1538-3881/153/1/37)
- Tanimura, H., Aghanim, N., Bonjean, V., Malavasi, N., & Doust, M. 2020, *A&A*, 637, A41, doi: [10.1051/0004-6361/201937158](https://doi.org/10.1051/0004-6361/201937158)
- Tanimura, H., Zaroubi, S., & Aghanim, N. 2021, *A&A*, 645, A112, doi: [10.1051/0004-6361/202038846](https://doi.org/10.1051/0004-6361/202038846)
- Tanimura, H., Hinshaw, G., McCarthy, I. G., et al. 2019, *MNRAS*, 483, 223, doi: [10.1093/mnras/sty3118](https://doi.org/10.1093/mnras/sty3118)
- Tejos, N., Prochaska, J. X., Crighton, N. H. M., et al. 2016, *MNRAS*, 455, 2662, doi: [10.1093/mnras/stv2376](https://doi.org/10.1093/mnras/stv2376)
- Tommasin, S., Spinoglio, L., Malkan, M. A., & Fazio, G. 2010, *ApJ*, 709, 1257, doi: [10.1088/0004-637X/709/2/1257](https://doi.org/10.1088/0004-637X/709/2/1257)
- Tommasin, S., Spinoglio, L., Malkan, M. A., et al. 2008, *ApJ*, 676, 836, doi: [10.1086/527290](https://doi.org/10.1086/527290)
- Tsvetanov, Z. I., & Petrosian, A. R. 1995, *ApJS*, 101, 287, doi: [10.1086/192241](https://doi.org/10.1086/192241)
- Tully, R. B., & Fisher, J. R. 1977, *A&A*, 54, 661

- Tumlinson, J., Peebles, M. S., & Werk, J. K. 2017, *ARA&A*, 55, 389, doi: [10.1146/annurev-astro-091916-055240](https://doi.org/10.1146/annurev-astro-091916-055240)
- Urban, O., Werner, N., Simionescu, A., Allen, S. W., & Böhringer, H. 2011, *MNRAS*, 414, 2101, doi: [10.1111/j.1365-2966.2011.18526.x](https://doi.org/10.1111/j.1365-2966.2011.18526.x)
- Vedantham, H. K., & Phinney, E. S. 2019, *MNRAS*, 483, 971, doi: [10.1093/mnras/sty2948](https://doi.org/10.1093/mnras/sty2948)
- Virtanen, P., Gommers, R., Oliphant, T. E., et al. 2020, *Nature Methods*, 17, 261, doi: [10.1038/s41592-019-0686-2](https://doi.org/10.1038/s41592-019-0686-2)
- Walker, C. R. H., Spitler, L. G., Ma, Y.-Z., et al. 2024, *A&A*, 683, A71, doi: [10.1051/0004-6361/202347139](https://doi.org/10.1051/0004-6361/202347139)
- Wang, P. F., Han, J. L., Xu, J., et al. 2023, *Research in Astronomy and Astrophysics*, 23, 104002, doi: [10.1088/1674-4527/acea1f](https://doi.org/10.1088/1674-4527/acea1f)
- Yao, J. M., Manchester, R. N., & Wang, N. 2017, *ApJ*, 835, 29, doi: [10.3847/1538-4357/835/1/29](https://doi.org/10.3847/1538-4357/835/1/29)